Universitetet i Stavanger

Faculty of Science and Technology

MASTER'S THESIS

Study program: **Marine and Offshore Technology**	Spring semester, 2021 **Open**
Author: **Grete Eiane (No. 253822)**	. . . . . . (Author's signature)

Faculty Supervisor:

Prof. Lin Li

Co Supervisor:

Filippos Kalofotias

Thesis title:

Hull Shape Optimization of Point Absorber Wave Energy Converters Using Open Source Programs

Credits (ECTS):

30

Keywords: Wave energy; Wave energy converter; Point absorber; Open-source program; Salome; Nemoh; Optimization; Integrated optimization process	Number of pages: 69 + Enclosure: 8 **Stavanger**, **14th of June 2021**

Abstract

Wave energy is harnessed during the transport and capture of waves at the ocean surface. It can potentially be a sustainable global energy source in the future. Wave Energy Converters (WEC) is one technology to generate electricity from waves. Many designs and concepts of WECs exist. Point Absorbers are one of these, and according to relevant studies, the most promising one.

The optimization of Wave Energy Converters (WECs) is a current topic related to the development of the ocean wave energy sector. This is of high interest between developers as competition is based on improving energy performance while reducing the cost. To solve the optimization problem, a numerical methodology is adopted in the present study. The optimization results reflect the Average Annual Power Absorption and the Levelized Cost of Energy (LCoE) of a WECs Point Absorber. Two constraints are applied; a constraint to achieve stability and a constraint to limit the heave motion. A cone and a bullet shape are considered, varying a set of design paramters. In total, one hundred geometries are genereated for each of the shapes.

The linear wave theory (LWT) is employed, and the open-source programs Nemoh and Salome are applied for the hydrodynamic computation. The aim of the study is to explore the use of these programs for hydrodynamics in terms of modelling, computational efforts and improvements in design optimization of WECs. A well-described method is presentented on how the open-soruce programs are connected to create an integrated optimization process to automate Salome and Nemoh.

Preface and acknowledgment

This master's thesis is written as a part of the two-year Master of Science program within Marine and Offshore Technology at the Department of Mechanical and Structural Engineering and Materials Science. The study was conducted at the University of Stavanger (UiS) during the spring semester of 2021.

From previous, I have bachelor within energy sources. The study programme focuses on renewables and I did my thesis on offshore wind energy. Therefore, I was intrigued that I got the chance to learn more about a renewale energy source that are not so well-established yet. However, it looks like it can have a signifcant contribution to the ever growing demand of energy.

I am very thankful for everything I have learned and gotten to experience over the past two years of my master's degree. I would like to thank my supervisor, Professor Lin Li, for trusting me with this project and continuous help, insight, and advice during the process. I would also like to thank my co-supervisor Filippos Kalofotias who put time and effort into guiding us through the work of the thesis and, arranging with workshops for tools that are used in the study. I am also very grateful for his sharing of knowledge on the topic of WECs.

Table of content

List of figures

List of tables

1 Introduction

1.1 Background and motivation

The global demand for energy increases rapidly. At the same time, most of the energy imports come from fossil fuels which contribute to global warming. One of the answers to overcome these problems lies in the exploitation of renewable energy sources (IEA, 2021).

Renewable energy sources are defined as 'inexhaustible' or sources that can be replenished in a short period. Examples are solar, wind, geothermal energy, hydropower, and wave energy. Wave energy applications are still in an early testing phase or pre-commercial stage compared to other, well-established renewable technologies (Antonio and reviews 2010).

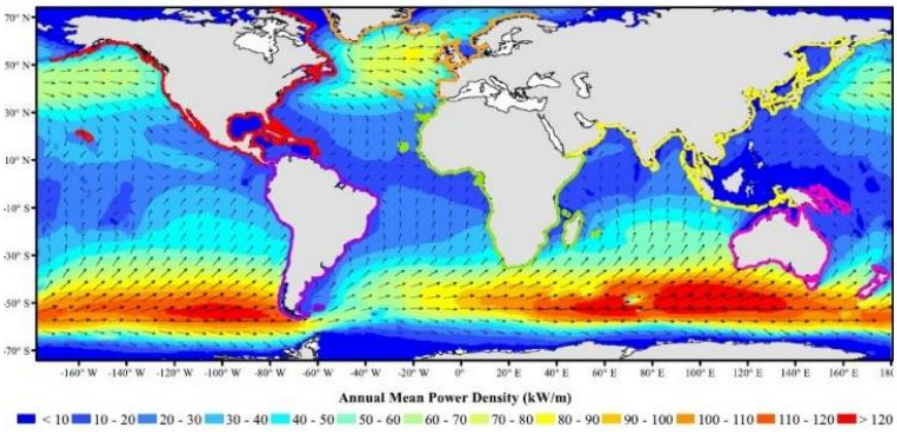

Figure 1 - Annual mean wave power density worldwide (Gunn and Stock-Williams 2012).

Even though the resource is not so well-established compared to other renewable recourses, it can contribute to clean energy production in the global energy demand. It is estimated that the global potential wave power resource is 2 TW in the world (Gunn and Stock-Williams 2012). Figure 1 is illustrating how the considerable potential of wave energy is globally distributed. Wave energy is harnessed during transport and capture by waves at the ocean surface. Hence, the waves are transformed into power from the movement in the water.

The harnessing of wave energy today is not yet commercially applied on a big scale. There are several challenges to overcome, making wave energy feasible. The challenge to efficiently

capture irregular motion has a significant impact on the design of the buoy. The floater and the power take-off system (PTO) system bust be rated for the most common wave power levels (Drew, Plummer et al. 2009). However, the design of the buoy should also consider withstanding extreme wave conditions (Clément, McCullen et al. 2002). The offshore environment leads to an increase in the cost of power transfer to shore and maintenance costs. (Kalofotias 2016) Challenges to overcome are also concerning the corrosive environment. On the other hand, the considerable potential that wave energy presents is a strong motive for more research on the topic. Thus, researchers must focus on the design to achieve more efficient ways of energy extraction.

1.2 Different types of WECs

Wave energy converters (WECs) are one technology that captures energy contained in ocean waves. The concept of harvesting energy from the ocean waves is not a new idea as the official patent of the first wave energy converter (WEC) was filed in Paris in 1799. Several hundreds of patents related to types of WEC's were present before the 20th century, mainly in the UK (Evans 1981). Even though the market for WECs is small compared to other renewable sources, many countries have experienced development within planning, installation, and operation of wave energy converts (Aderinto and Li 2018). There are significant variations in the design and concepts of WECs. Despite the considerable variation in designs and concepts, WECs can be classified into three predominant types.

Terminator

Terminator devices have their principal axis parallel to the wavefront (perpendicular to the predominant wave direction) and physically intercept waves. The Salter's DuckIt is an example of a terminator-type WEC. Figure 2 is illustrating the concept of Salters Duck. During the impact of waves, the duck rotates the gyroscopes inside to provide electrical energy through a generator (Mueller, Baker et al. 2001).

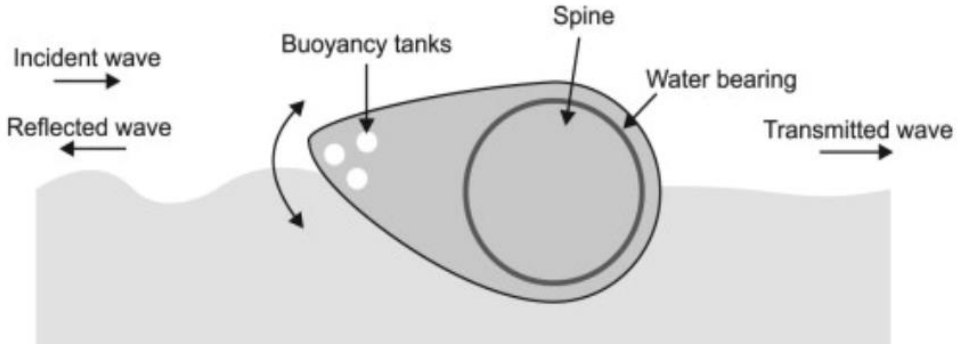

Figure 2 - Sketch of Salter's Duck (Salter 1974).

Attenuator

Attenuators lie parallel to the predominant wave direction (Drew, Plummer et al. 2009). One example of an attenuator is the Pelamis, see Figure 3. It can remind of a snake in the sea. The device is made up of several floating cylindrical segments joined together by hinges.

Figure 3 - Pelamis wave energy converter (NNMREC 2015).

Point absorber

The present study is based on point absorber type WEC. An illustration photo of a point absorber WEC is shown in Figure 4. The dimension of a point absorber WEC is smaller relative to the incident wavelength (Vantorre, Banasiak et al. 2004). The point absorber can harvest wave energy from waves larger than the dimensions of its structure itself (Thomas 2008). As a result, they can be more cost-effective in terms of manufacturing, installation, and maintenance. They oscillate with the ocean waves with one or more degrees of freedom (Faizal, Ahmed et al. 2014). There are numerous examples of point absorbers. Figure 5 is illustrating a basic design concept of a point absorber WEC.

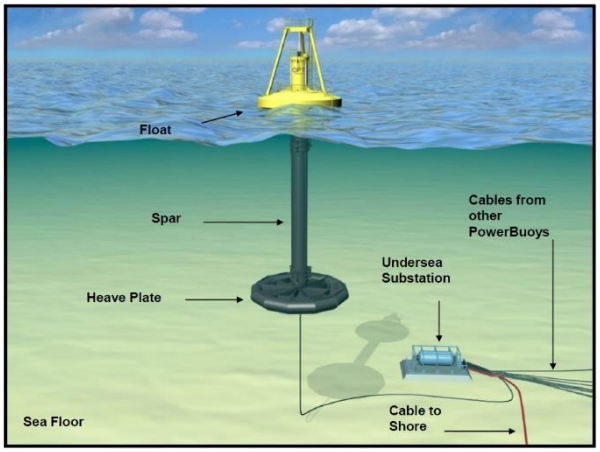

Figure 4 - Illustration photo of point absorber WEC

Figure 3 illustrates the fundamental working concept of a point absorber system. Point absorbers are devices that are using floating bodies to absorb waves. The buoy is floating on the sea surface. Below the buoy is a hydraulic cylinder fixed to the seabed. It utilizes a cable or a pillar to secure its floating. Wave excitation force drives the buoy, providing motion between the piston connected to the buoy and the cylinder. Between the buoy and the seabed, there is a so-called power take-off (PTO) system. This mechanical device is used to capture the induced motion of the floater, and hence, through an automated generator (damper), it transforms it into electrical power. The mechanical spring of the point actuated device is also used to hold the system in line.

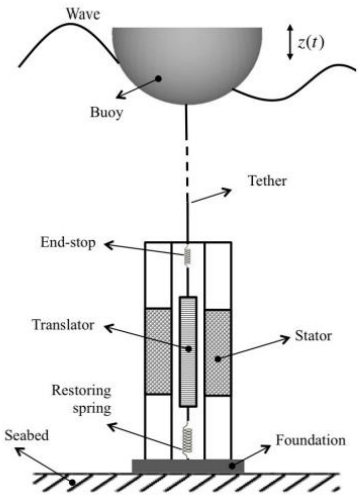

Figure 5 - Basic design of a point absorber WEC (Wahyudie, Jama et al. 2015).

1.3 Literature review

The report of Kalifatios studied the design optimization and modeling improvement of a point absorber. The shape and dimensions of the hull of the point absorber were considered regarding design optimization. Three different shapes were evaluated; cylinder, bullet, and cone. Based on the results from Kalifatios, the present thesis will establish the design of the geometries on the bullet and the cone shape. Specific restrictions regarding maximum dimensions of the hull were applied, but only a small selection of geometries was considered. The following work will include a significant selection of varying design parameters. The dimensioning of the three shapes from Kalifatio is similar to the present study, conducted by building a model deriving the average power extraction of each design in the frequency domain. To obtain the result, the Boundary Element Method (BEM) uses 3D diffraction theory in the open-source program Nemoh.

Boundary Element Methods (BEM) are becoming increasingly important to investigate interacting point absorbers with current computer capacity. (Ricci, Lopez et al. 2011) compared results obtained with a BEM code to the point absorber approximation and optimized the point absorber geometry.

Some studies have been carried out to optimize different point absorber types in recent years to improve energy absorption efficiency. (Sergiienko, Neshat et al. 2020) performed a research on WEC design optimization for the wave climate at Albany test site in Western Australia considering unidirectional irregular waves. The study did only consider a vertical cylinder shape. By the results of Kalifatios thesis, the present study is considered geometries that The present study is comparing to offshore sites in the North Sea.

1.4 Aim and scope

The present study aims to perform a set of analyses obtaining information to find the desired design of the hull shape of a point absorber WEC. Two European offshore sites will be applied to compare how the energy performance is distributed for different sea states. Two objective functions will be maximized/minimized to obtain the result of the optimization problem. The first objective function will analyze the absorbed power, whereas the goal is to maximize the energy output.

Further, the economic aspect will be integrated to make the design of the WEC cost-effective. Thus, the second objective function will be calculating the Levelized Cost of Energy (LCoE), whereas the goal is to minimize the cost. Two constraints will further be applied to the WEC system. The first constraint will make sure that the floating body is stable. In the second, a stroke restriction will be implemented to reduce the heave motion amplitude of the buoy.

The aim of the study is to explore the use of open-source programs Salome and Nemoh for hydrodynamics for design optimization of WECs. The open source programs are connected to create an integrated optimization process to automate Salome and Nemoh for X_N geometries.

Two different shapes will be evaluated to perform the work presented above. For both shape, a fixed set of dimensions is created by varying the radius and the draft of the hull shape. An illustration of both figures can be seen in Figure 6, namely (a) cone (b) cullet. All necessary design parameters and boundaries are presented in Chapter 3.

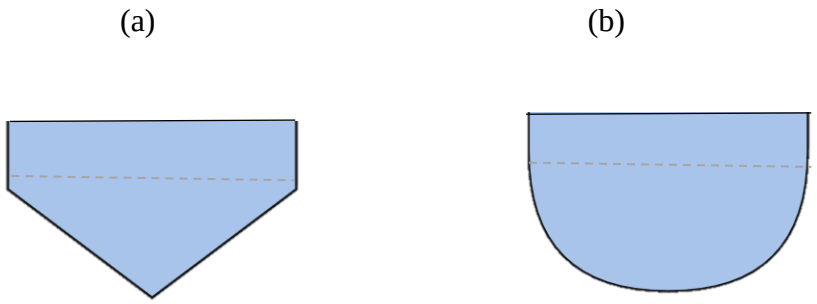

Figure 6 - Illustration of evaluated geometries

1.5 Outline of thesis

The thesis is constructed according to the scientific research model IMRaD. A short description of every chapter is presented below.

Chapter 1: An introduction is given to get an understanding of the topic and today's situation. The focus of the chapter is to establish an overview of the work done in the thesis.

Chapter 2: The relevant theory of ocean waves and wave energy extraction is presented and utilized in the following chapters.

Chapter 3: The numerical method is described concerning design variables, objective functions, and constraints. Furthermore, a presentation of the open-soruce programs is given or the thesis and how they are utilized.

Chapter 4: The results from the conducted research are presented. The results include the objective functions and compare the constrained and unconstrained results.

Chapter 5: The final chapter presents the main conclusions of the work and provides a brief suggestion for further work.

2 Theory

2.1 Navier Stoke equation

The Navier-Stokes equations (NSE) are considered to fully describe the dynamic of fluid motion. Consider a cartesian coordinate system (x,y,z) with the z-axis pointing vertically upwards and the origin located in the quiescent free surface. By assuming irrotational flow, it can be described as the gradient of the velocity potential. We can treat the flow to be inviscid because the viscous effect is limited to the boundary layer. The equation of continuity for incompressible fluids, the velocity potential, will satisfy the following equation:

$$\frac{\partial u}{\partial x}+\frac{\partial v}{\partial y}+\frac{\partial w}{\partial z}=0 \qquad \text{Eq. 1}$$

For inviscid fluids, the Navier-Stokes equations can be simplified, resulting in Euler equations. By adopting the Eulerian approach, The NSE is based on the conservation of momentum and the conservation of mass.

Conservation of mass

$$\vec{\nabla} * \vec{u} = 0 \qquad \text{Eq. 2}$$

Conservation of momentum

$$\frac{\partial \vec{u}}{\partial t} + (\vec{u} * \vec{\nabla})\vec{u} = -\frac{1}{\rho}\vec{\nabla}p + v\vec{\nabla}^2\vec{u} + F_b \qquad \text{Eq. 3}$$

Where:

$\vec{u}$ *= the water particles velocity vector: (u,v,w) [m/s]*

v *= the components velocity vector in x-,y-,z-direction [m/s]*

ρ *= the water density [kg/m^3]*

p *= the point pressure [N/m^2]*

v *= kinematic viscosity of water [m^2/s]*

F_b *= the gravity vector [0,0-g] [m/s^2]*

g *= the acceleration of gravity [m/s^2]*

The equation for conservation of mass determines that the volume and mass remain constant. Theconservation of momentum is a representation of Newton's 2nd law. The first term on the left-hand side of the equation represents the acceleration of water particles. The second term is the forces acting on the surface of the fluid. While in the right-hand side, the first term is the pressure acting on the fluid and affection of surrounding conditions. The second term is the shear forces acting on the fluid, while the last term includes the external forces acting on the fluid. Solving the equation allows for a detailed explanation of the fluid field. However, no analytical solution of the full NSE is yet to be derived. As a result, several assumptions and boundary conditions are adopted, making the Linear Wave Theory (LWT). For further information about NSE, the reader can refer to Kundu et al. (2012) and Anderson (1995).

2.2 Linear Wave Theory

Linear wave theory (LWT), also known as potential theory, is a simplified description of fluid motion and is the most widely applied and helpful theory. It is a simplified approximation to the NSE, where the second term on the right-hand side of Eq. 3 is neglected. The simplification gives a good approximation of wave characteristics for a wide range of wave parameters. During the

design of offshore structures, this theory can provide a reliable estimation while in an early phase of comparing different designs.

In this study, an approximation of hydrodynamic forces acting on the WEC is calculated using LWT. This theory is valid for small amplitude waves compared to their wavelength and water depth. Moreover, extreme waves are not considered. In these situations, the WEC most likely must stop producing energy to prevent fatigue of the WEC. For a valid application of LWT, the water must be assumed to behave as an irrotational fluid. It is considered a negligible viscosity, a constant density, and the fluid must be incompressible (Journée and Pinkster 1997). It allows for the introduction of the velocity potential according to:

$$\frac{\partial \phi}{\partial x} = u, \qquad \frac{\partial \phi}{\partial y} = v, \qquad \frac{\partial \phi}{\partial z} = w \qquad \text{Eq. 4}$$

LWT is valid only for sinusoidal wave solutions of the ocean surface, and for any other shape, LWT is not applicable. The sinusoidal waveform can be expressed:

$$\zeta(x,t) = \zeta_a \cos(kx - \omega t) \qquad \text{Eq. 5}$$

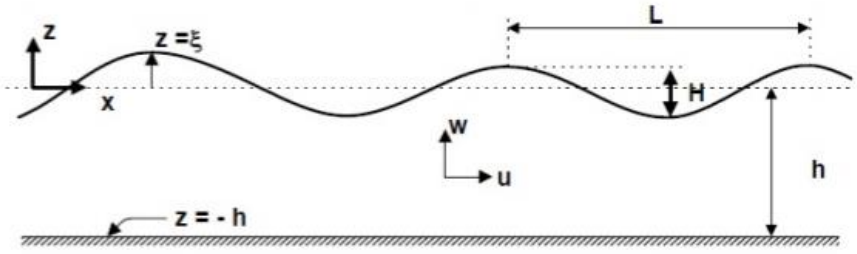

Figure 7 - Sinusoidal waveform

Where:

$\zeta(x,t)$ *= the free surface elevation with respect to z = 0 [m]*

ζ_a *= the free surface elevation amplitude*

k = the wave number [rad/m]

ω = the free surface oscillation angular frequency [rad/s]

As mentioned, several assumptions are made, making the linear wave theory valid. Another assumption is that the wave height, H = $2\zeta_a$ is assumed to be significantly smaller relative to the incident wavelength L and water depth h. However, these high amplitude waves carry more energy, meaning that these high amplitude waves are essential for wave energy converters. The mentioned assumption is necessary for introducing the linearization of the Bernoulli equation and for the gradient of the second term in Eq. 3. to be small enough to be neglected. For a detailed derivation of the expression of LWT, the reader can refer to chapter 5 of Journée and Massie (2001). To sum up, the LWT can provide results in a relatively short time. It can contribute to a consistent yet rough design estimation during an early phase. During the calm wave conditions, the LWT happens to be quite accurate.

2.3 Wave energy

Linear wave theory (LWT) allows measuring the amount of energy transfer during waves for two conditions. The first is energy transfer under regular (sinusoidal) waves, while the second condition of energy transfer is under irregular waves as those observed in reality

2.3.1 Energy transfer in regular waves

The following chapter is considering a sinusoidal wave, as shown in Figure 2. The highest point of a wave is called its crest, and as a sine wave describes the wave, its amplitude will equal the distance from the still water level to the crest.

For a sinusoidal wave, the following relation account for amplitude, ζ_a:

$$H = 2\zeta_a^2 \qquad \text{Eq. 6}$$

The distance between any two wave crests is the wavelength, denoted as λ, while the distance along the time axis is the wave period: T.

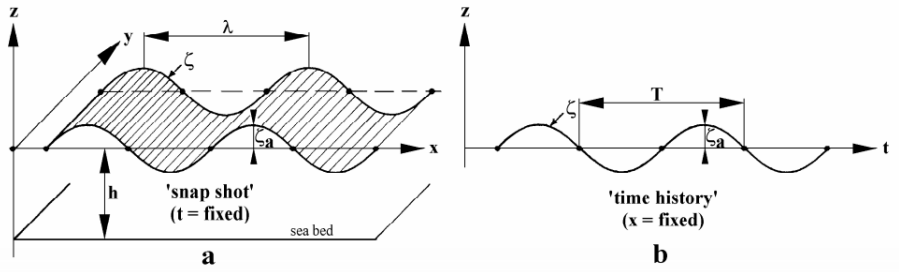

Figure 8 - Harmonic wave

The wave speed, c, follows from:

$$c = \frac{L}{\lambda} = \frac{\omega}{k} \qquad \lambda = \frac{2\pi}{k} \qquad T = \frac{2\pi}{\omega} \qquad \text{Eq. 7}$$

The wave speed, c, is the speed for one individual wave. This speed is, in general, smaller compared to the velocity of a group of several waves. Each amplitude envelope contains a group of internal waves; hence this speed is typically named group velocity. The following expression calculates it:

$$c_g = c * n \qquad \text{Eq. 8}$$

Where n can be found from:

$$n = \frac{1}{2}\left(1 + \frac{2kh}{\cosh 2kh}\right) \qquad \text{Eq. 9}$$

The total wave energy consists of both potential and kinetic energy. Therefore, the sum of the potential and the kinetic (total energy) is derived as:

$$E_{total} = E_{kinetic} + E_{potenial} = \frac{1}{4}\rho g\zeta_a^2 + \frac{1}{4}\rho g\zeta_a^2 = \frac{1}{8}\rho g H^2 \qquad \text{Eq. 10}$$

Where:

E_{total} *= the total energy per unit surface area [J/m^2]*

$E_{kinetic}$ *= the kinetic energy of water particles unit surface area [J/ m^2]*

$E_{potential}$ *= the potential energy of water particles unit surface area [J/ m^2]*

At last, by combining the equations from the chapter, the average power output can be calculated. The Power from the waves or the average energy transfer over one wave cycle per unit wave crest is expressed as:

$$\bar{P} = E_{total} * c_g \qquad \text{Eq. 11}$$

2.3.2 Energy transfer in irregular waves

Every range of frequency exists for the open sea, and waves of the sinusoidal forms are rarely observed. The ocean surface appears to be a superposition of random waves of various lengths and periods. The wave energy spectrum was created by simplifying the wave energy spectrum, making it possible to estimate the energy transfer during sea states composed of several wave frequencies. There exist several different types of wave spectrum, and for the present study, the JONSWAP spectrum is applied.

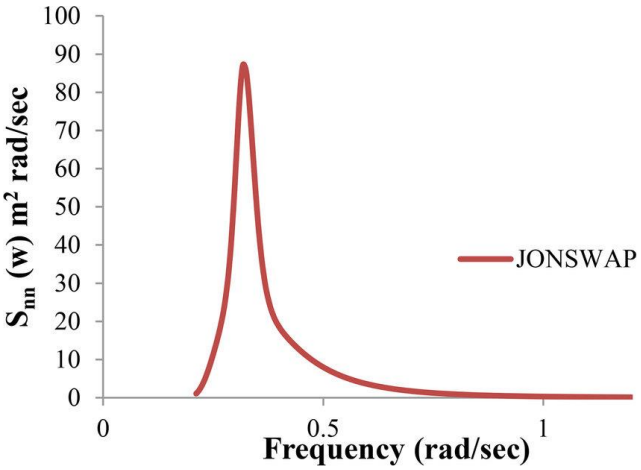

Figure 9 - Wave spectrum (JONSWAP)

The statistical properties of the irregular sea state are described by the frequency-dependent energy density relation, $S_\zeta(\omega)$. The graph in Figure 9 is the energy density spectrum for a given sea state, $S_\zeta(\omega)$ (red line), plotted against the range of frequencies.

The energy density, $S_\zeta(\omega)$, can be calculated according to:

$$S_{\zeta(\omega_n)} * \Delta\omega = \frac{1}{2}\zeta_{a_n}^2 \qquad \text{Eq. 12}$$

Where:

$S_{\zeta(\omega_n)}$ *= the energy density value corresponding to the frequency* ω_n *[*m^2s*]*

$\Delta\omega$ *= the frequency interval [rad/s]*

ζ_{a_n} *= the wave amplitude corresponding to the frequency* ω_n *for the respective energy contribution*

The JONSWAP spectrum was established during a research project called "Joint North Sea Wave Project" in 1967 to conduct wave measurements in the North Sea. It is an extension of the Pier Moskowitz-spectrum, extended to include fetch limited seas (Hasselmann, Barnett et al. 1973). The wave spectrum is never fully developed; it will continue to grow in non-linear wave interactions for long distances and times.

The formula of the JONSWAP spectrum is given by:

$$S_\zeta(\omega) = 320\ \frac{H_s^2}{T_p^4}\omega^{-5}\exp\left(\frac{-1950}{T_p^4}\omega^{-4}\right)\gamma^A \qquad \text{Eq. 13}$$

$$A = \exp\left(-\left(\frac{\frac{\omega}{\omega_p}-1}{\sigma\sqrt{2}}\right)^2\right) \qquad \text{Eq. 14}$$

Where:

H_s = significant wave height, the average of the highest 1/3 of the wave height record [m]

T_p = peak period corresponding to the frequency corresponding to the frequency ω_p with the highest energy density [s]

γ =3.3 (peakedness factor)

σ = a step function of ω: if $\omega \leq \omega_p$ then $\sigma = 0.07$

a step function of ω: if $\omega \geq \omega_p$ then $\sigma = 0.09$

ω_p = the peak frequency corresponding to the highest energy density value of the spectrum [rad/s]

The total energy per unit surface area in an irregular sea state equals the area under the JONSWAP graph multiplied by ρg. The formula for total energy yields:

$$E_{total} = \rho g \int_0^\infty S_\zeta(\omega)d\omega \qquad \text{Eq. 15}$$

2.4 Hydrostatic stability

A floating body reaches its state of equilibrium when the resultant forces and relative moments equal to zero. According to the Archimedes law, it states the following:

$$F_{\nabla} = pg\nabla \quad \text{Eq. 16}$$

Where:

$F_{\nabla} = buoyancy\ force$

$pg\nabla = density\ of\ water \cdot gravity \cdot Submerged\ volume\ of\ a\ floating\ body$

The buoyancy force is equivalent to the gravitational force of the body. Equilibrium is achieved according to Archimedes principle that holds that the gravitational force mass m multiplied by gravity g can be denoted as:

$$mg = pg\nabla \quad \text{Eq. 17}$$

Thypothetical points determine the hydrostatic stability of a floating body. It includes the center of gravity (CoG), the center of buoyancy (CoB), in addition to the length between the keel and the CoB. Figure 10 is illustrating the concept of stability. The gravitation forces act around the point of CoG. The point is marked as 'G' in Figure 10 and is described as the point where the combined mass of the floating structure is concentrated.

The CoB is defined as the center of volume of the submerged part of the floating body, marked as 'B' in Figure 10. The properties of CoB and CoG are used to determine the height between the metacenter, denoted as M in the figure, and the CoG. M is the point where the vertical line from the original CoB point will intersect the vertical line for a heeled CoB. (Biran and Pulido 2013)

$$\overline{GM} = \overline{KB} + \overline{BM} - \overline{KG} \quad \text{Eq. 18}$$

$$COG = \frac{\sum m_n z_n}{\sum m_n} \quad \text{Eq. 19}$$

$$COB = \frac{\sum \rho g \nabla_n z_n}{\sum \rho g \nabla_n} \quad \text{Eq. 20}$$

$$\overline{BM} = \frac{I}{\nabla} \quad \text{Eq. 21}$$

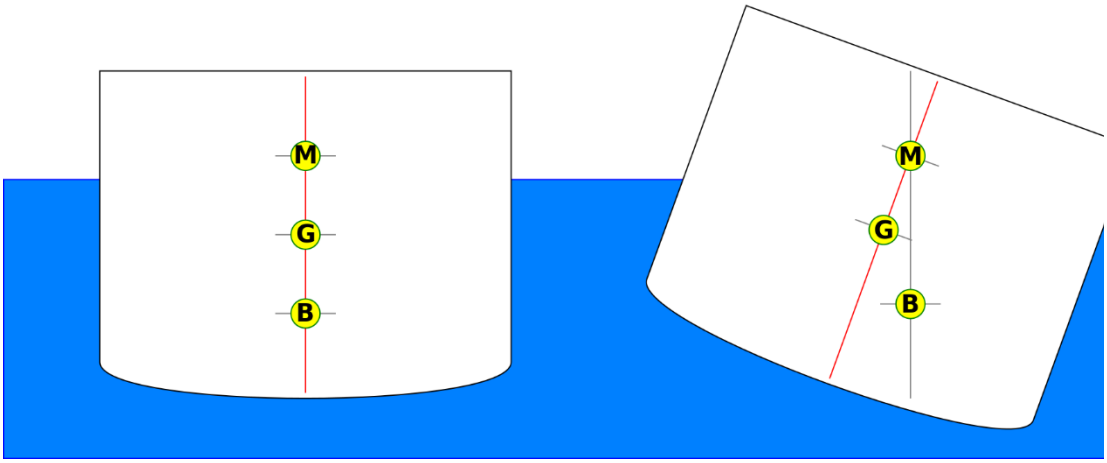

Figure 10 - Hydrostatic stability

2.5 Linear mass-spring-damper system model (MSDS)

Loads on a floating object can be either constant in time, transient or harmonic, whereas the motion response for these loads is fundamentally different. In early design phases, linear approximation allows random or irregular loads to be treated as a superposition of harmonic loads. Commonly, the motion of most floating structures can be described by the widely applied mass-spring-damper-system (MSDS). The following equation describes it for small motions and linear behavior. The derivation of the MDSDS system analyses the moments and

forces are acting on the floating body. A floating object has six degrees of freedom in total, three translational and three rotational concerning the x-y,-, z-axis.

A structure that is floating freely in a short-crested sea will oscillate in six degrees of freedom. More specifically, three translational and three rotational degrees of freedom with respect to the x-y,-, z-axis. Figure 11 illustrates the different motions. For this study, the heave motion will be of significant importance. Hence, the heave motion will be the motion of direction to include, deriving the calculations for the hydrodynamic forces.

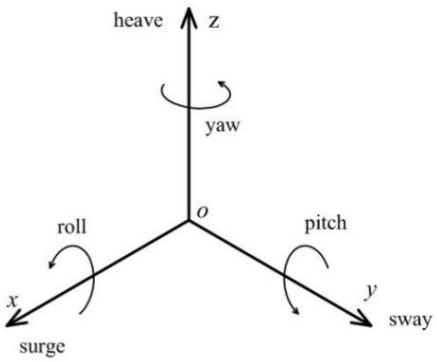

Figure 11 - 6 DOF wave motion

• z1, surge in the longitudinal x-direction, positive forwards,

• z2, sway in the lateral y-direction, positive to port side,

• z3, heave in the vertical z-direction, positive upwards

• z4, roll about the x-axis, positive right turning

• z5, pitch about the y-axis, positive right turning

• z6, yaw about the z-axis, positive right turning

Some structures are not freely floating but are restrained to fewer degrees of freedom due to, e.g., their connection to the seabed. For instance, the point absorber considered in the present

study is restrained from heaving motion only. This means that the derivation of the MSDS model will be derived for one degree of freedom in the heave direction to analyze the forces acting on the floating body. In general, the forces acting on a floating structure are described below.

Added mass, F_{add}

For floating structures in water, the mass inertia is increased by an added mass or a hydrodynamic mass. The added mass of the buoy is caused by the accelerating force needed to move the volume of water surrounding the floating body. This added mass coefficient is proportional to the acceleration of a linear system.

Damping force, F_{rad}

The oscillations of a floating body will generate waves. These waves carry energy, meaning that they withdraw energy from the buoy's oscillations, and its motion will die out. This is the damping coefficient in the linear MSDS system and is proportional to the velocity of the floating structure.

Restoring spring coefficient, F_{res}

For a structure oscillation in water, it displaces an amount of water equal to the submerged volume of the structure. According to Archimedes law, $F_{buoyancy} = pg\nabla$, which is proportionate to the magnitude of the buoyancy force. The restoring spring force is applied until it reaches equilibrium.

Wave excitation force, F_{exc}

The diffraction problems describe excitation forces acting on the floating body in a fixed position. The buoy's pressure field is disrupted, causing a disturbance from the hydrostatic state; this is the Diffraction force. The integration of the pressure on the body in undisturbed waves is the so-called Froude-Krylov force. These make up the non-viscous forces acting on the floating body in regular waves.

The total forces acting on a floating body can be then be expressed by the following formula:

$$F_{total} = m\ddot{z} = F_{exc} + F_{add} + F_{rad} + F_{res} \qquad \text{Eq. 22}$$

Extending the formula for the forces acting on the body from Eq. 22, the equation of motion yields:

$$(m + a)\ddot{z} + b\dot{z} + cz = \dot{F}_{excitation} \quad \text{Eq. 23}$$

Where:

$a =$ *an added mass coefficient [kg]*

$b =$ *a radiation damping coefficient [kg/s]*

$c =$ *a restoring coefficient [kg/s^2]*

$\ddot{z} =$ *the vertical acceleration of the floating body[m/s^2]*

$\dot{z} =$ *the velocity of the vertical displacement of the floating body [m/s]*

$z =$ *the vertical displacement of the floating structure [m]*

For a 6 DOF system, the 6x6 matrices for the added mass, mass, radiation coefficient, and spring coefficient are denoted in Eq. 24 to Eq. 27.

The zero terms in the matrices are due to the symmetry of the geometry of the buoys. As a result of the symmetric geometry, C_{44} will equal C_{55}. C_{33} is the coefficient of interest in this study since RAO is calculated in heave motion. The spring coefficient will be the same for both geometries with a fixed diameter as the waterline areas are alike for both the cone and the cylinder for each unique dimension and is calculated according to:

Added mass matrix

$$a = \begin{bmatrix} a_{11} & 0 & 0 & 0 & a_{15} & 0 \\ 0 & a_{22} & 0 & a_{24} & 0 & 0 \\ 0 & 0 & a_{33} & 0 & 0 & 0 \\ 0 & a_{42} & 0 & a_{44} & 0 & 0 \\ a_{51} & 0 & 0 & 0 & a_{55} & 0 \\ 0 & 0 & 0 & 0 & 0 & a_{66} \end{bmatrix} \quad \text{Eq. 24}$$

Mass matrix

$$m = \begin{bmatrix} m_{11} & 0 & 0 & 0 & 0 & 0 \\ 0 & m_{22} & 0 & 0 & 0 & 0 \\ 0 & 0 & m_{33} & 0 & 0 & 0 \\ 0 & 0 & 0 & I_{44} & 0 & -I_{46} \\ 0 & 0 & 0 & 0 & I_{55} & 0 \\ 0 & 0 & 0 & -I_{64} & 0 & I_{66} \end{bmatrix} \quad \text{Eq. 25}$$

Damping coefficient matrix

$$b = \begin{bmatrix} b_{11} & 0 & 0 & 0 & b_{15} & 0 \\ 0 & b_{22} & 0 & b_{24} & 0 & 0 \\ 0 & 0 & b_{33} & 0 & 0 & 0 \\ 0 & b_{42} & 0 & b_{44} & 0 & 0 \\ b_{51} & 0 & 0 & 0 & b_{55} & 0 \\ 0 & 0 & 0 & 0 & 0 & b_{66} \end{bmatrix} \quad \text{Eq. 26}$$

Restoring spring coefficient

$$c = \begin{bmatrix} 0 & 0 & 0 & 0 & 0 & 0 \\ 0 & 0 & 0 & 0 & 0 & 0 \\ 0 & 0 & c_{33} & 0 & c_{35} & 0 \\ 0 & 0 & 0 & c_{44} & 0 & 0 \\ 0 & 0 & c_{53} & 0 & c_{55} & 0 \\ 0 & 0 & 0 & 0 & 0 & 0 \end{bmatrix} \quad \text{Eq. 27}$$

2.5.1 Power Take-Off (PTO)

In addition to the forces acting on a floating body generally, additional forces act on the specifically chosen type of WEC point absorber. It includes the mechanical spring force, k, and the PTO damping coefficient β. These coefficients will be assumed adjustable and steady per sea state, as applied by Kao (2014).

Mechanical spring force, F_{sp}

A mechanical spring is connected to the floating body and the PTO to ensure the system stays in line, restoring spring force. The optimum value of k yields:

$$F_{sp} = \; k = \omega_p^2 \left[m + a(\omega_p) \right] - c \quad \text{Eq. 28}$$

PTO Damping force, F_{pto}

The floating body of the point absorber is connected to the damper of the PTO device. This will harness the energy from the wave, generating electricity. The optimum values of β can be calculated as:

$$F_{pto} = \beta = \sqrt{b(\omega_p)^2 + \frac{1}{\omega_p^2}\left(-\left(m + a(\omega_p)\right)\omega_p^2 + c\right)^2} \qquad \text{Eq. 29}$$

The optimal damping coefficient of the PTO is calculated based on a PTO system that is illustrated in Figure 12. The PTO converts the energy absorbed in the buoy into electricity. The PTO affects the amount of wave energy absorbed, the size, the mass, and the structural dynamics of the wave energy converter. (Hansen, Andersen et al. 2011) .

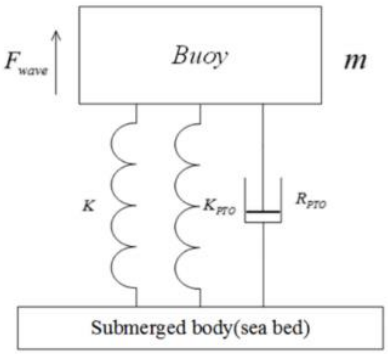

Figure 12 - PTO system for WEC

In LWT, viscous forces are not taken into account. Hence the hydrodynamic results based on computer programs using only LWT are insufficient to calculate the floater response.. In hydrodynamic analysis, several approaches can be applied to account for viscous effects. The method used here is to use a small percentage of the critical damping, which is expressed as:

$$b_{cr} = 2\sqrt{(m + a) \cdot c} \qquad \text{Eq. 30}$$

Where m_{ij} is the mass term, a_{ij} is the added mass term and c_{ij} is the restoring spring term. The non-hydrodynamic damping is calculated as a fraction of the critical damping b_{cr}.

By introducing the coefficients for the mechanical spring force and the PTO damping force to the equation of motion from Eq. 22 can be rewritten:

$$F_{total} = m\ddot{z} = F_{exc} + F_{add} + F_{rad} + F_{res} + F_{spring} + F_{pto} \quad \text{Eq. 31}$$

Extending the formula for the forces acting on the WEC, Eq.23 can be rephrased as:

$$(m + a)\ddot{z} + (b + b_{cr} + \beta)\dot{z} + (c + \dot{k})z = F_{exc} \quad \text{Eq. 32}$$

Where:

k *=a mechanical spring coefficient [kg/s^2]*

β *=PTO damping coefficient [kg/s]*

2.6 Response Amplitude Operator (RAO)

The system is characterized in terms of a transfer function for a floating body, assuming linear behavior. The absolute value of the transfer function is the response amplitude operator. The RAOs are the ratio between the response of the floater, in motion in one of the six degrees of freedom, and the amplitudes of the incoming waves, which is the solution of the MSDS model in the frequency domain. The spectra are proportional to the amplitude squared, and thus, they can be derived from the motion and wave spectra. The ratios between the motion spectra and the incoming waves' spectra denote the transfer function, the RAO squared.

The mathematical description of RAO yields:

$$RAO(\omega) = \frac{F_{exc}(\omega_n)}{\sqrt{\left[c + k_{sp} - [m + a(\omega_n)] * \omega_n^2\right]^2 + [b(\omega_n) + \beta + b_{cr}]^2 \omega_n^2}} \quad \text{Eq. 33}$$

2.7 Short term analysis of floater response

Short-time sea states are characterized by the significant wave height and spectral peak period. The JONSWAP wave spectrum defines these parameters. The response spectrum, which

statistically describes the response process for a linear process, can be determined from the wave spectrum and the response amplitude operator in the following way:

$$S_{xx}(\omega) = RAO(\omega)^2 S_\zeta(\omega) \qquad \text{Eq. 34}$$

Spectral moments are calculated by

$$m_x = \int_0^\infty \omega^x \, S_{xx}(\omega) \qquad \text{Eq. 35}$$

The numbers of zero-crossing response cycles in a 3-hour sea state are given by

$$n_{3h} = \frac{10\,800\ s}{t_{m0}} \qquad \text{Eq. 36}$$

From spectral moments we can calculate the variance and the zero-up-crossing period for the response process with the following equations:

$$t_{m0} = 2\pi \sqrt{\frac{m_2}{m_0}} \qquad \text{Eq. 37}$$

The distribution function of the 3-hour maximum response amplitude is given by:

$$F_{X_{3h}} = \left[1 - exp\left\{\frac{1}{2}\left(\frac{x}{\sigma_x}\right)^2\right\}\right]^{n_{3h}} \qquad \text{Eq. 38}$$

The characteristic largest response value, $\tilde{x}3h$, is defined as the expected level exceeded once per 3 hours. By assuming Rayleigh distribution, the value for $\tilde{x}3h$ can be estimated from the expression:

$$\tilde{x}3h = \sigma_x \sqrt{2 \ln(n_{3h})} \qquad \text{Eq. 39}$$

2.8 Power Extraction

The force-generating electrical power is the PTO damping force, F_{pto}. The needed velocity is simply the buoy's velocity, leading to the expression for the instantaneous power absorption.

$$P(t) = F_{pto} z(t) \quad \text{Eq. 40}$$

The generated power is harnessed by the PTO damping force and can be calculated by the following expression:

$$\overline{P} = \frac{1}{2} F_{pto}(\omega_n) \omega_n^2 RAO(\omega_n) \zeta_{an}^2 \quad \text{Eq. 41}$$

N is the number of frequency components and is dependent on the frequency range. The average extracted power is the superposition of the regular wave components in an irregular sea state. It results in an average power extraction for each of the geometries for the different sea states.

3 Methodology and numerical method

3.1 Formulation of design problem

The proposed integrated optimization method is applied to the geometry of the design of the WEC point absorber. The analysis problem seeks to either minimize or maximize a given function, known as an objective function. For a general optimization problem, Eq.42 can be considered (Li, Jiang et al. 2019).

Maximize: $f_1(x)$ Eq. 42

Minimize: $f_2(x)$

Subject to: $g_i(x)$ $i=1,\ldots n; \quad x^L < x < x^U$

Where f_1 and f_2 are the objective functions to maximize and minimize, g_i is the constraint function; x is the design variable vector. x^L and x^U are the lower and upper bounds of the design variables, respectively.

Methods for solving the equations play an essential role in finding the solution to these objective functions. Two objective functions, denoted as f1 and f2, are presented in the present study to design the most favorable WEC. First, the geometries must be geometrically described for deriving the optimized dimension of every design. The following section will present the design variables and introduce the objective function and the applied constraint for the design problem.

3.1.1 Design variables

Based on relevant literature, two different shapes will be evaluated, and both shapes will be created, varying a set of parameters. The geometries applied are shown in Figure 13, namely (a) cone and (b) bullet. The design variables will include two independent variables: the radius,

R of the buoy, and the height, H, of the cylindrical part of the buoy. Both the cylinder and the bullet are composed of an upper cylindrical part. The cone has a conical lower part pointing downwards, while the bullet shape is formed of a hemispherical lower part. The height of the lower part will equal the R of the buoy. Though. The total height is the sum of R and H and makes up the total draft of the geometries, denoted as TD. Based on the present geometrical description, a set of designs of variable dimensions are produced for every shape. Every set of designs is made by varying the radius, R, and the cylindrical height, H. As mentioned earlier in the thesis, the design parameters are restricted within a range of upper and lower boundaries. These are presented in chapter 3.1.3.

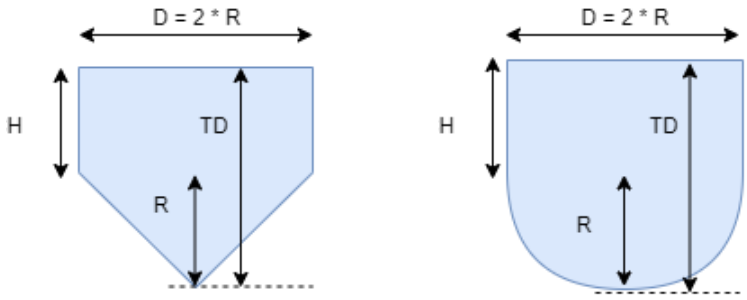

Figure 13 - Sketch of gemoetries with design variables, R and H for (a) cone (b) bullet

3.1.2 Objetive function

Objective function *1*, f_1

The first function will evaluate the energy performance by calculating the mean annual absorbed energy. Next, the absorbed energy will be summarized for all operational sea states to find the average yearly energy absorption. Finally, the occurrence for all sea states will be summarized and divided to obtain an average value. Thus, the function of a given geometry and sea state under random spectral conditions can be written as:

$$\overline{P}_{AAP} = f_1 = \frac{1}{\left|\hat{O}(H_s, T_p)\right|} \sum_{H_s} \sum_{T_p} \hat{O}(H_s, T_p)\, \overline{P}(H_s, T_p) \qquad \text{Eq. 43}$$

where $\hat{O}(H_s, T_p)$ is the annual occurrence of each operational sea state with significant wave height, H_s, and mean zero up-crossing periods, T_p. H_s stands for the significant wave height, i.e., the average of the highest 1/3 of the waves during a specific sea state. T_p stands for the zero up-crossing periods of the waves, i.e., the average time for the surface elevation to cross zero by upward motion twice. $\overline{P}(H_s, T_p)$ is the extracted power for the corresponding sea state. The extracted power can be expressed by Eq. 42 from Chapter 2.8 Power Extraction.

$$\overline{P}(H_s, T_p) = \frac{1}{2} F_{pto}(\omega_n)\omega_n^2 RAO(\omega_n)\zeta_{an}^2 \qquad \text{Eq. 44}$$

The annual energy production of each geometry is in the North Sea to represent the device's performance. For the wave energy resource, irregular unidirectional waves in a non-fully developed sea are represented by the JONSWAP spectrum presented in Chapter 2.3.2 Energy transfer in irregular waves. The sea states and sites that are applied for the calculations will be presented in 3.1.4.

Objective function *2*, f_2

The second objective function will calculate the Levelized Cost of Energy (LCoE). This number measures the average net present cost of electricity generation for a generating plant over its lifetime. LCoE will be calculated based on reasonable assumptions from previous research. A study (de Andres, Maillet et al. 2016) concluded that the LCoE for CorPower devices, which is of a WEC point absorber, can be approximated by the following equation:

$$f_2 = LCoE\left(\frac{Price}{MWh}\right) = \left(\frac{Energy(MWh)}{Mass(kg)}\right)^{-0,5} \qquad \text{Eq. 45}$$

$$f_2 = LCoE\left(\frac{€}{MWh}\right) = \left(\frac{f_1 * 8760\frac{hours}{year}}{m_{buoy}}\right)^{0,5} \qquad \text{Eq. 46}$$

The goal of wave energy conversion is to produce the highest annual energy production while at the same time minimizing the LCoE. Thus, the purpose of having the present objective functions are to:

(i) Maximize the average annual power output specified Eq. 43

(ii) Minimize the value of LCoE using Eq. 46

3.1.3 Design constraints

Design boundaries

For avoiding over-dimensioning of the WEC, some design restrictions are applied for upper and lower boundaries. The radius, R, ranges from 5 meters to 20. The height of the cylindrical part of the buoy, H, will be evaluated within limits ranging from 1 meter to 5 meters. Based on these numbers, the total draft of the buoy ranges from 6 to 25 meters. These upper and lower boundaries are based on an optimal full-scale dimension of WEC point absorber technologies for average northern European wave conditions (Pecher and Peter Kofoed 2017). The geometries are illustrated in Figure 4 with the corresponding variables, while upper and lower boundaries are presented in Table 1.

Table 1 - Upper and lower boundaries for design variables

Variable	**Symbol [m]**	**Lower boundary , X^L**	**Upper boundary, X^U**
Radius	R	5	20
Height (cylindrical part)	H	1	5

Stability constraint

The stability of the buoy is an essential factor in the design phase. Stability is achieved through effectively designing the mass distribution by a metacentric height (GM), ensuring the buoy remains in stable equilibrium. If a floating body is stable, it means that it returns to its equilibrium while being displaced. The minimum value for GM in the present thesis is set to

be equal to or greater than 1.0 m for the buoy to be stable. The formula for stability is calculating using Eq. 18:

$$g_1(x) = \overline{GM} = \overline{KB} + \overline{BM} - \overline{KG}, \quad \overline{GM} \geq 1 \qquad \text{Eq. 47}$$

Heave motion restriction

A stroke constraint is implemented on the floater, imposing a maximum value on the significant amplitude of the body motion. The constraint of a stroke restriction will limit the heave motion. The theory for the floater response was presented in Chapter 2. In practice, point absorbers are likely to have some limits on the buoy motion to avoid fatigue on the system. The maximum height for the buoy to move in an upwards direction is set relative to the cylindrical part of the buoy and should not exceed the value assigned to 2H. The x̃3h value is calculated using Eq. 39.

$$g_2(x) = \tilde{x}3h = \sigma_x\sqrt{2\ln(n_{3h})}, \quad \tilde{x}3h \leq 2H \qquad \text{Eq. 48}$$

3.1.4 Limitations and assumptions

The buoy of the WEC is restricted to a single degree of freedom, more specifically in heave (displacement in the z−direction). Heave motion is the beneficial motion for wave energy conversion.

All coefficients calculated for the point absorber in heave motion are the optimal values. In reality, there will always be some losses in the PTO device, in which the result of the coefficient values is somewhat inaccurate. Restrictions regarding the PTO generator have not been considered, and potentially different control strategies have not been included in the design or modeling phase. It is assumed to provide damping forces to the mechanical system with a linear behavior.

Linear wave theory is a simplified description of fluid motion that is a widely applied theory and has a significant practical application. The theory is based on several assumptions and

appropriate boundary conditions for an analytical solution to be derived. Neither any mooring lines nor other environmental loads are considered in this project.

3.1.5 Site condition

The wave climate is determined from the scatter diagram (Li, Gao et al. 2015) for potential European offshore sites. The two marked areas (1) 14. Norway 5 and (2) 15. North Sea Center is chosen, and a selection of 40 sea states is considered in the present study for comparison. It covers five values of H_s ranging from 0.5 to 4.5 m and eight T_p values ranging from 3.0 to 10.0 s. The corresponding scatter diagrams for site 1 and site 2 are presented in Table 2 - Scatter diagram for sea states for site: Norway 5 and Table 3 - Scatter diagram for sea states for site: North Sea Center, respectively. The occurrence for each of the sea states is the number in the cells of the tables.

Sea states with significant wave heights lower than or equal to 4.5 meters will be considered in this thesis. All the above sea states are regarded as non-operational. Consequently, the WEC will shut down under these conditions to avoid fatigue on the PTO system.

Since the JONSWAP wave spectrum is used to describe waves of the North Sea, the spectrum is chosen to represent the offshore sites for the present study and was introduced in Chapter 2. The reader can refer to

Figure 14 - Overview over European offshore sites. 14. Norway 5 and 15. North Sea center is eveluated in the present thesis.

Appendix A – Python codingfor insight into the python script for the JONSWAP spectrum.

Table 2 - Scatter diagram for sea states for site: Norway 5

Hs [m]/Tp [s]	3.0	4.0	5.0	6.0	7.0	8.0	9.0	10.0
0.5	0	0	16	0	2	6	0	19
1.5	8	320	480	804	1417	1576	1927	2317
2.5	0	2	318	1052	875	1041	1706	2238
3.5	0	0	1	181	693	794	674	940
4.5	0	0	0	4	106	383	582	487

Table 3 - Scatter diagram for sea states for site: North Sea Center

Hs [m]/Tp [s]	3.0	4.0	5.0	6.0	7.0	8.0	9.0	10.0
0.5	996	1342	325	157	213	253	120	113
1.5	76	3431	6884	4645	2548	1137	667	1111
2.5	0	3	834	4387	1888	869	518	209
3.5	0	0	2	402	2089	557	287	180
4.5	0	0	0	1	433	614	261	154

3.2 Numerical method and open-source program

Chapter 3.2 and 3.3 will include information about the numerical method and the open-source program applied in the present thesis and how they are utilized and connected. All the calculations performed from these programs are calculated by self-made scripts made by the author of the thesis. The reader can refer to the Appendix A for insight in coding.

3.2.1 Open-source program Salome

Salome is an open-source software providing a platform for numerical simulation. The geometries in the present study are modeled using Salome. The software provides a generic and efficient user interface, which uses an open and flexible architecture of reusable components. The software supports interoperability between CAD modeling and computational software; hence it can be used as a standalone feature for the generated CAD models in preparation for numerical simulations. Further, Salome can be used to create the mesh for CAD models and export the mesh data. Thus, generated mesh models can export to the preferred format for either pre or post-processing. (SALOME, 2016).

3.2.2 Establishing 3D meshing

The modeling of the geometries in Salome is presented in Figure 16 - 3D - CAD model of and Figure 15 - 3D - CAD model of . The axis level is set to the surface level (z=0), meaning that the geometries are totally submerged. All geometries are axis-symmetric around the x-axis

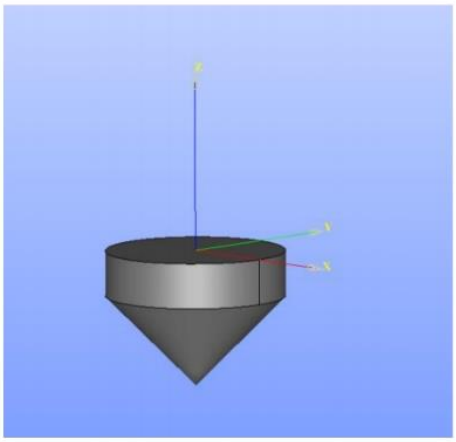

Figure 16 - 3D - CAD model of cone

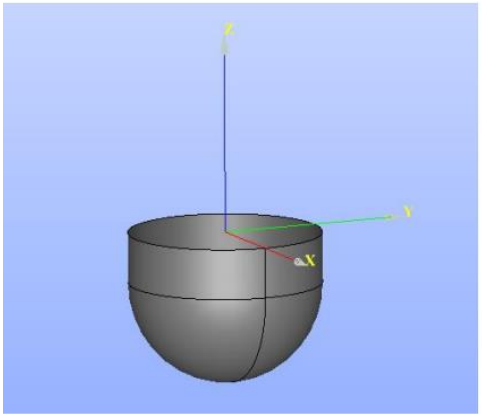

Figure 15 - 3D - CAD model of bullet

and y-axis. Hence, the axis is set in the middle of the structure. Furthermore, the z-axis is pointing upwards, negative direction towards the draft of the buoys.

The meshed surfaces are shown in Figure 18 and Figure 17. The meshes are divided into panels, whereas the center of each panel has a known coordinate. The panel method is an analysis method that can be used to get an approximate solution for the forces acting on an object in a flow. As we present it here, the process is based on inviscid flow analysis, so it is limited to the resultant pressure forces over the surface.

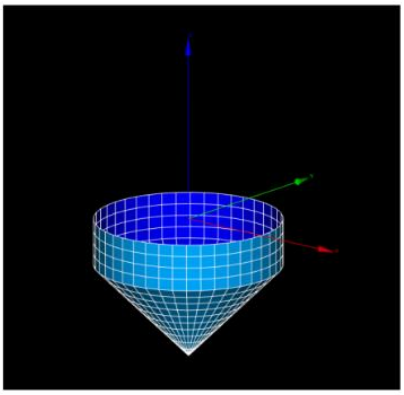

Figure 18 - Meshing of cone

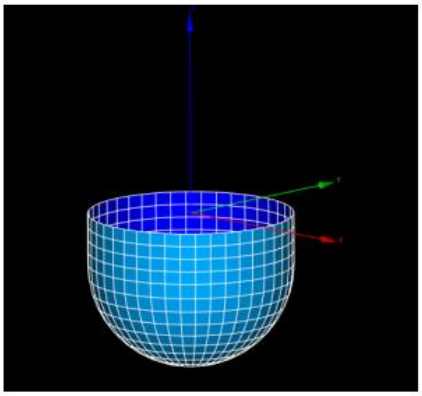

Figure 17 - Meshing of bullet

The panel model will be selected to calculate the hydrostatic and hydrodynamic forces from potential buoys' potential theory. In this case, quadrangular panels with four nodes are used for both geometries, with a panel size of 1.0 m. This positioning is used as input for the Nemoh calculations. For all panels, both the radiation and diffraction problems are solved. The total range of a discrete force is calculated for the integration of pressure for every panel.

3.2.3 BEM in Nemoh

In this report, the Boundary Element Method (BEM) model used is NEMOH. (Ecole Centrale de Nantes, 2016). This is the first open-source BEM code, being available since 2014. The BEM model is a linear model used for hydrodynamic input to the Frequency Domain. Nemoh is used to solve the three-dimensional radiation and the diffraction problems, such as added mass, radiation, damping, and excitation forces in the frequency domain by taking advantage

of linear 3-D-Diffraction Theory. (Babarit and Delhommeau 2015). For a detailed description of the three-dimensional-diffraction theory, the reader can refer to chapter 7 of the paper of Journee and Massie (2001). Nemoh uses the panel method to compute wave loads and hydrodynamic characteristics of bodies interacting with ocean surface waves. The number of panels should be large enough for a good accuracy regarding the size of the geometry. Water is considered an ideal fluid, and viscous effects are neglected. Furthermore, the interactions between the structure and its surrounding water are assumed to be linear. Ther reader can refer back to Chapter 2 for more basic thoery.

Nemoh is composed of three sets of programs that are intended to run in sequent order:

- preProcessor - reads and prepare the exported .DAT file and calculates cases with the stated body conditions. The .DAT-file includes all information about the mesh.

The preProcessor aims to prepare the mesh and generate the body conditions for each calculation case (radiation and diffraction). Calculation cases are defined in the input file Nemoh.cal, which must be located in the working folder.

- solver - solves the linear BVP with linear wave theory for stated body condition and calculates hydrodynamic coefficients: added mass, damping
- postProcessor - processes the results and which is used for further relevant calculations

The postProcessor aims to post-process the results to provide the relevant quantities (added mass, radiation damping, excitation force) in the usual format. In addition, it provides a framework to make appropriate calculations, i.e., calculating RAO. Once it runs successfully, results files are created and stored in the working folders including the radiation coefficients, diffraction force and excitation force

A reasonable number of frequencies have been used for the hydrodynamic simulation, ranging between 0.1 and 3.0 rad/s with steps of 0.05. The excitation and radiation problem will be solved for the chosen frequency interval.

3.2.4 Programming language

Spyder is an open-source integrated development environment (IDE) for scientific programming in the Python language. It was initially created and developed by Pierre Raybaut in 2009. Since 2012, Spyder has been improved, developed continually, and maintained by scientific developers within the community. Spyder includes plugins such as SciPy, Matloblib, and NumPy, which include tools for advanced problem-solving.

3.3 Integrated optimization method

Figure 19 shows the flow of how the integrated optimzation is done. It allows for the open-soruce programs to connect and obtain results for every geometry. The process is explained in detail for the next section.

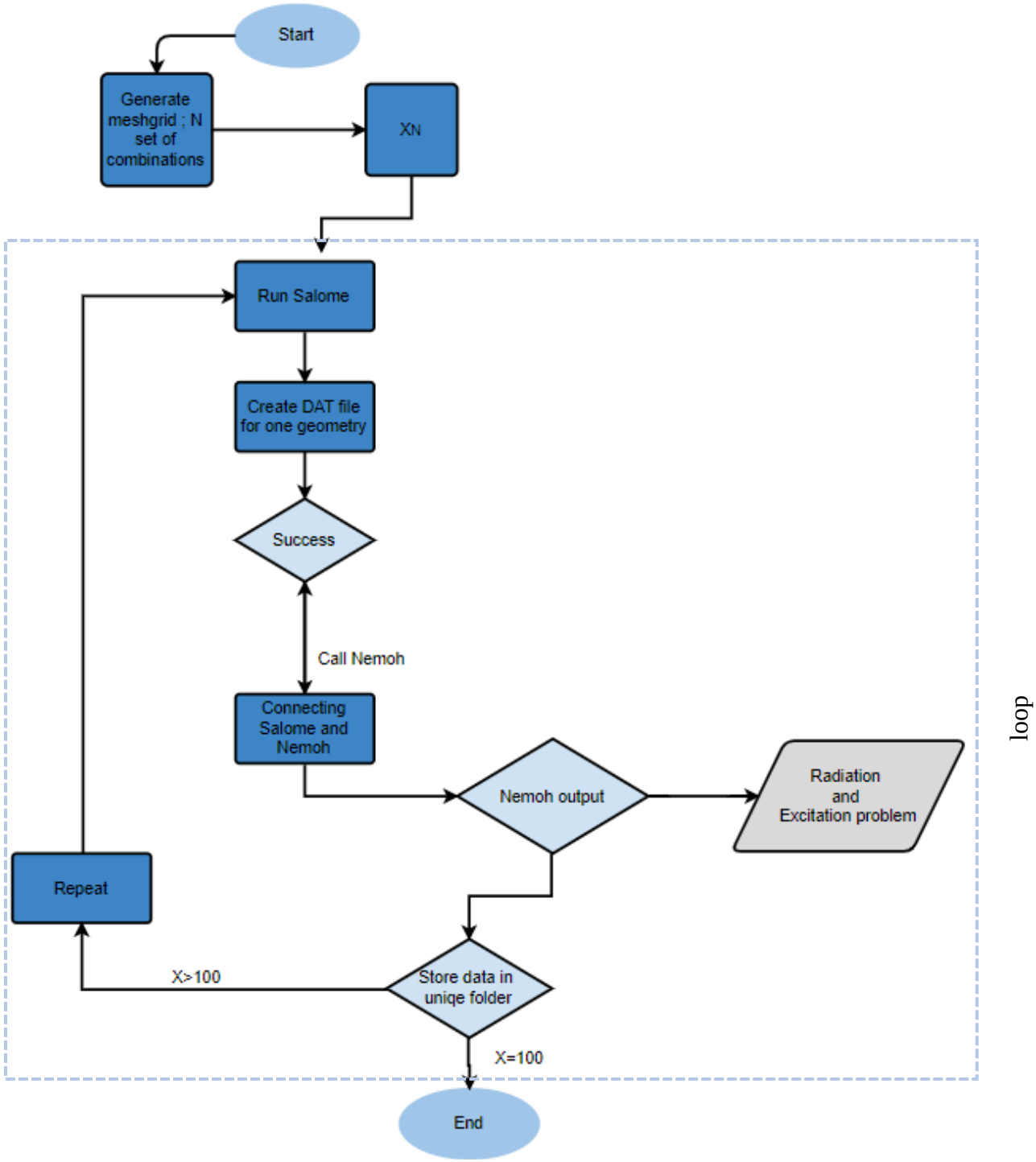

Figure 19 - Flowchart diagram for the process of Nemoh and Salome automation

3.3.1 Nemoh and Salome connection

At first, a mesh grid is created in Python within the boundaries for the geometries. A Python script is designed to run Salome and solve Nemoh automatically. Hence, the script allows Salome to run and export the mesh file (.DAT-file) for all the generated geometries. Once the .DAT file is successfully exported, Nemoh can automatically solve the radiation and diffraction problems by automatically calling the subprocess function in Python. The process is repeated in a loop for 100 different geometries for both the bullet and the cone. The script can easily be adjusted to any geometry, and changing the mesh grid can generate results for any number, $X_{N,}$ and size of the geometry.

A input file for Nemoh is created for general properties. The following file contains information about gravity, seawater density. It automatically calculates the center of gravity concerning the radius and height by implementing a python script with necessary mathematical formulas. This file must be located in the working folder and copied into every Result folder for each produced geometry.

As soon as the results for one geometry are calculated, the results are saved in a unique folder, namely Results1. Once it is done, it will move on to the following geometry, whereas the results will automatically be stored in folder Results2. The loop will continue until it completes the results for the 100th geometry. It gives a rather fast solution, depending on the number of frequencies, the size of panels.

The process of the Salome and Nemoh automation can be summarized in the flowchart diagram in Figure 19. The whole process from start to end is based on one programming script created for the present study.

The results from the hydrodynamic simulations from Nemoh are now stored as text files in the folder system. Several Python scripts are created to sort out the added mass, damping coefficients, and the excitation force to use the data further. Python sorts the data to solve for 6 DOF, consequently giving the frequency-dependent excitation forces for all 6 DOF in addition to coefficients in the 6 DOF matrices for damping and added mass coefficients. Hence, providing the opportunity to solve radiation and diffraction problems for 6 DOF, even though the present study is solved only for heave motion. The reader can refer to Appendix A for insight into the script of this process.

4 Results and discussion

Chapter 4 will include the results obtained from the conducted analyses. The results are divided into hydrodynamic properties, optimization results and comperative study for site 1 and 2.

4.1 Results on the hydrodynamic properties

The following section will include the results from the hydrodynamics, considering both the bullet and the cone shape. The coefficients of the added mass, a(ω), damping coefficients, b(ω), and the excitation force, $F_{exc}(\omega)$ for heave motion are introduced and compared. Further on, the results for the derived RAO are presented with and without critical damping.

The coefficient is essential to the dynamic response because it influences the resonance properties of the buoy and its wave-making capacity. The following analysis will examine how the dimensions of the buoy can affect power extraction.

Figure 20 illustrates how the added mass varies with the increased radius and fixed height of the cylindrical part of the geometry. The following sections are including buoys of **(1)** R=5 m, **(2)** R= 6 m, **(3)** R=8m, and **(4)** R=10 m.

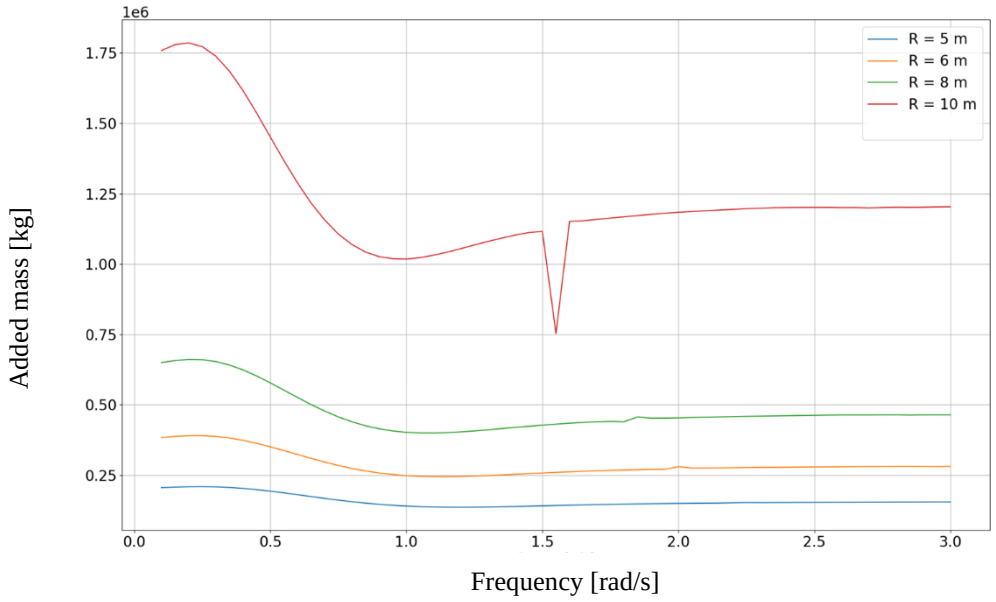

Figure 20 - Added mass, a(ω), for varying R - bullet

There is a clear correlation between the radius and the result of added mass. The coefficient, a(ω), will increase while the radius of the buoy increases. It is similar to the findings of Kalifatios (2016). However, the added mass for increased cylindrical height will decrease the added mass for low frequencies.

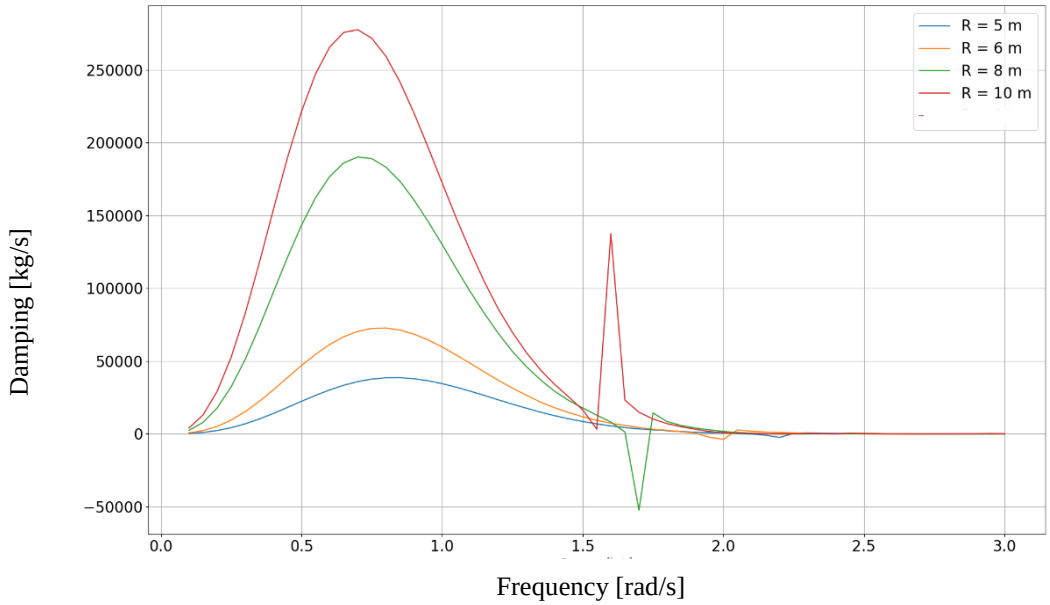

Figure 21 - Damping, b(ω), for varying R - bullet

The result of the damping coefficient, b(ω), is presented in Figure 21. The most significant difference in damping among the geometries is frequencies ranging from 0.5 rad/s to 1.0 rad/s.

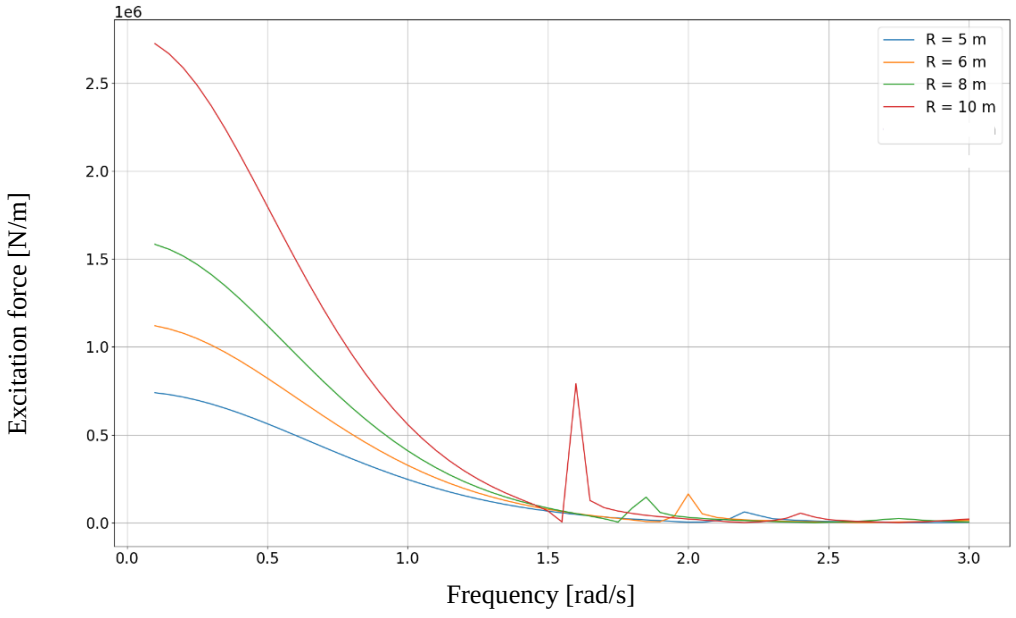

Figure 22 - Excitation force, Fecx (ω), for varying R - bullet

Similar to the added mass, a similar correlation is found for the damping coefficients. Increased radius leads to an increase in the damping of the floating body. In contrast, the increased draft of the buoy and a fixed radius will decrease the damping.

Figure 24 displays the excitation force, F_{ecx} (ω). The excitation force follows the same trend as both a(ω) and b(ω). The excitation forces are larger for buoys with larger radius. It especially accounts for frequencies in the lower range. The excitation force is almost alike for frequencies above 1.0 rad/s.

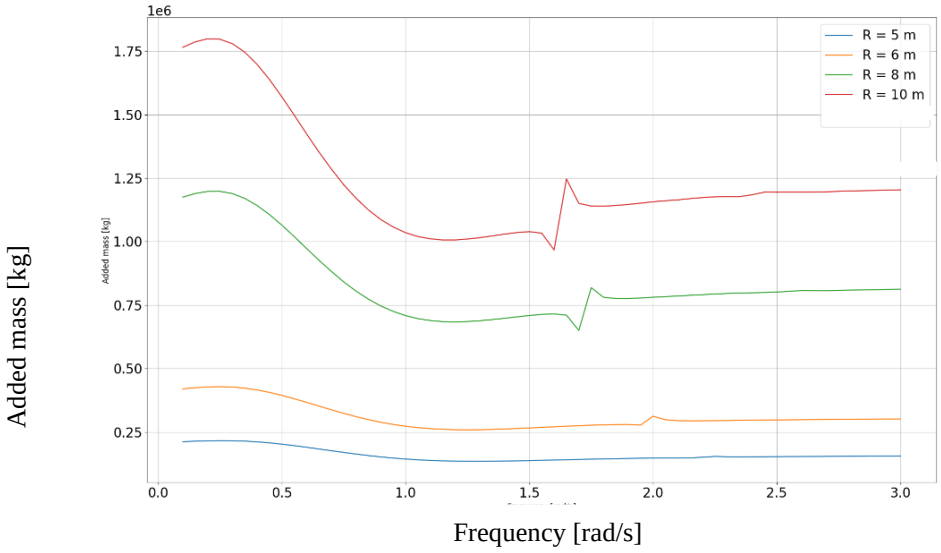

Figure 23 - Added mass, a(ω), for varying R - cone

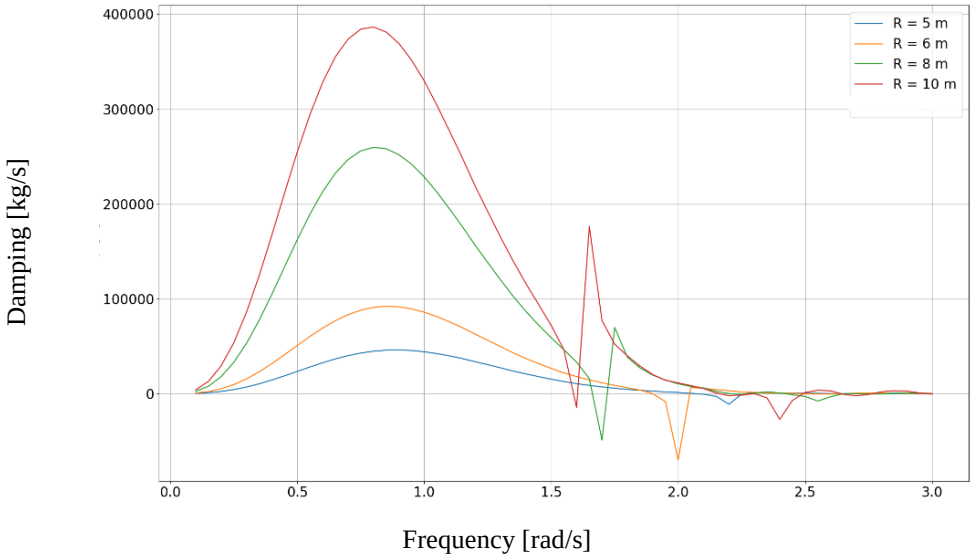

Figure 24 - Damping, b(ω), for varying R - cone

The same analysis is presented for the cone, whereas the hydrodynamic results show the same trend for the bullet and the cone regarding added mass, damping, and excitation force.The added mass, a(ω), for the cone is displayed in Figure 23 above. The damping coefficient, b(ω), for the cone is presented in Figure 24. Lastly, the graph of excitation force, Fexc(ω), is shown in Figure 25.

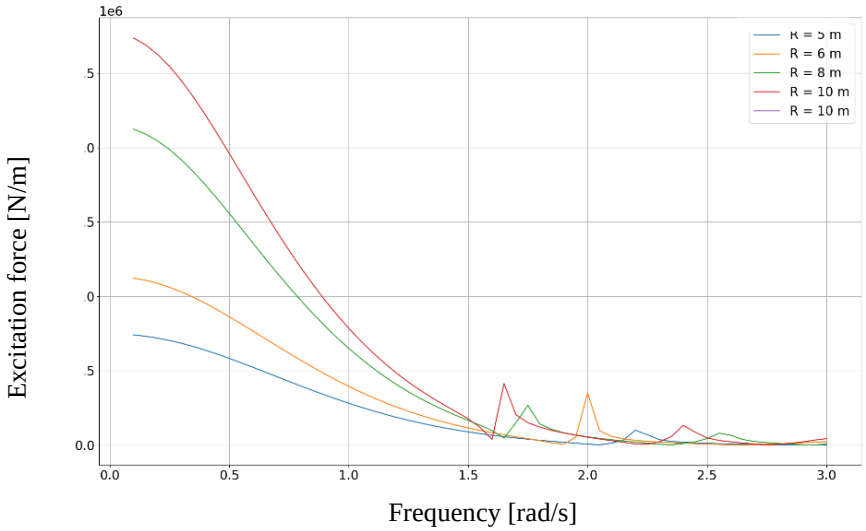

Figure 25 - Excitation force, Fecx (ω), for varying R - cone

Comparison of bullet and cone

The following analysis will compare the coefficients obtained from Nemoh is for the cone and bullet. In Figures 26, 27 and 28 the hydrodynamic added mass, damping coefficients, and the excitation forces for heave for both the bullet and the cone are presented, respectively. The hydrodynamic added mass, damping coefficient, and excitation force for the cone buoy are higher than the bullet shape.

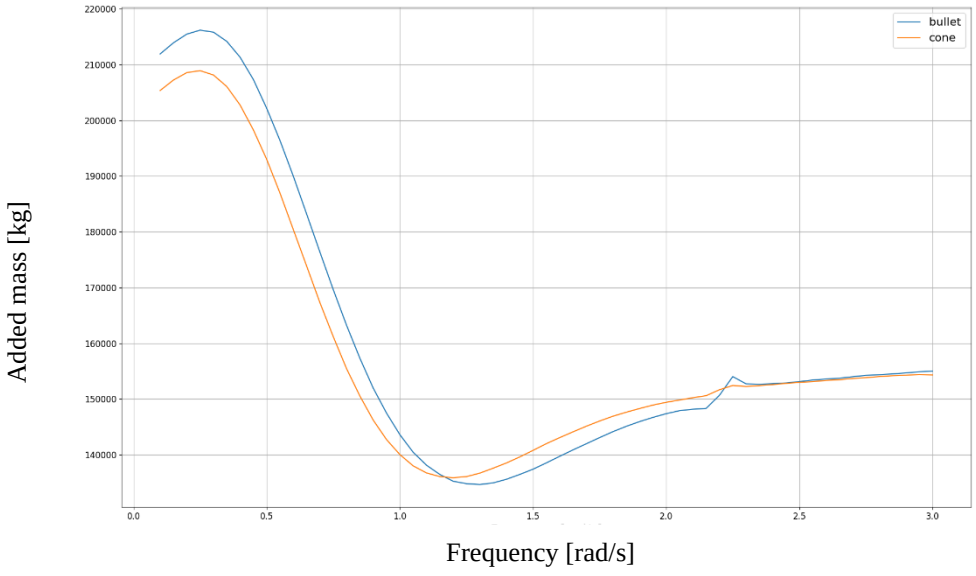

Figure 26 - Added mass, a(ω), for cone and bullet

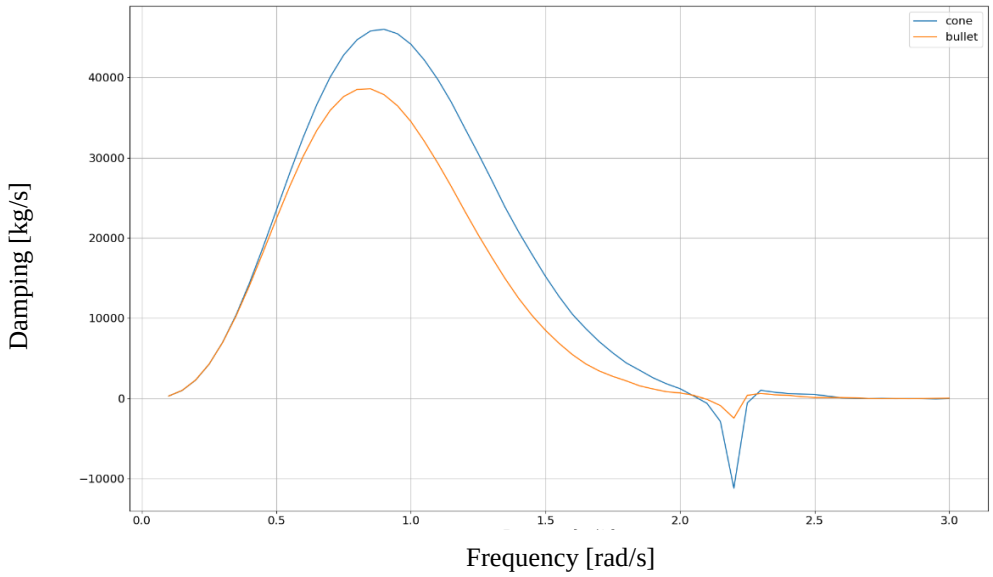

Figure 27 - Damping coefficients, b(ω), for cone and bullet

The results indicate that the cone shape is the better wave absorber compared to the bullet shape. As a result of the more significant radiation damping coefficients, b(ω) for the cone, it is expected that the cone will radiate more energy than the bullet for the same oscillation. The cone is exposed to larger excitation forces, especially for frequencies between 0.5 and 2.8 rad/s. Theses of Kalfatios (2016) can support the results, whereas the results are similar for the shape of the floater.

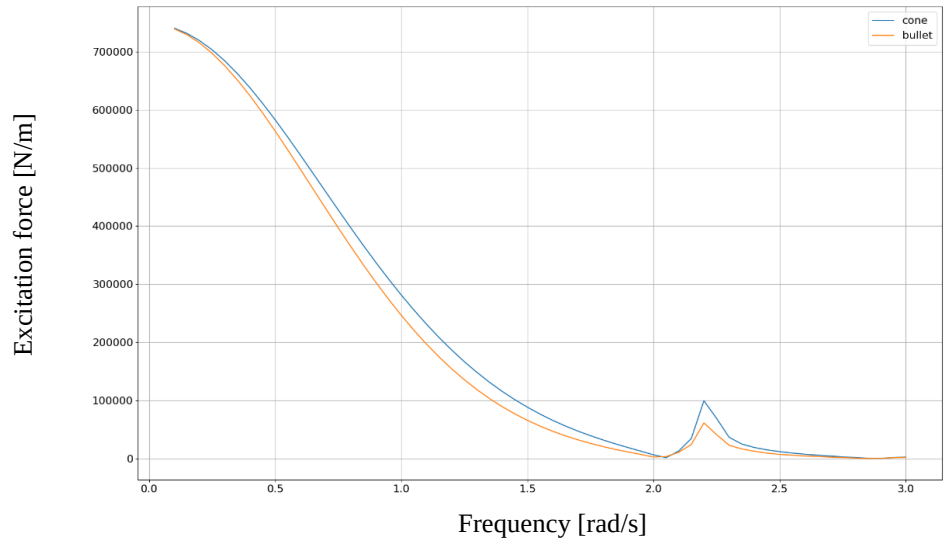

Figure 28 - Excitation force, Fecx (ω), for cone and bullet

The hydrodynamic results can also be supported by the calculations of (De Backer 2009).In both theses, the cone was the shape with the highest hydrodynamic results for added mass, damping, and excitation force. The results were further derived to obtain the RAO for both the cone and the bullet.

Response Amplitude Operator (RAO)

The RAO for four geometries of the bullet shape is presented in the following section. The values for RAO are calculated using Eq.33, and are assumed to be reasonable. In a study (Zhou, Hu et al. 2020) on motion response and energy conversion performance of a heaving point absorber WEC the RAO for several dimensions for both the bullet and cone shapes were calculated. It gives the values for RAO, whereas the relation between the radius and draft indicates the approximate belonging peak values. In general, the RAO achiece a lower peak for higher radius. Figure 29 shows the RAO value for four geometries without critical damping, while Figure 30 shows the value of RAO for the same four geometries including critical damping.

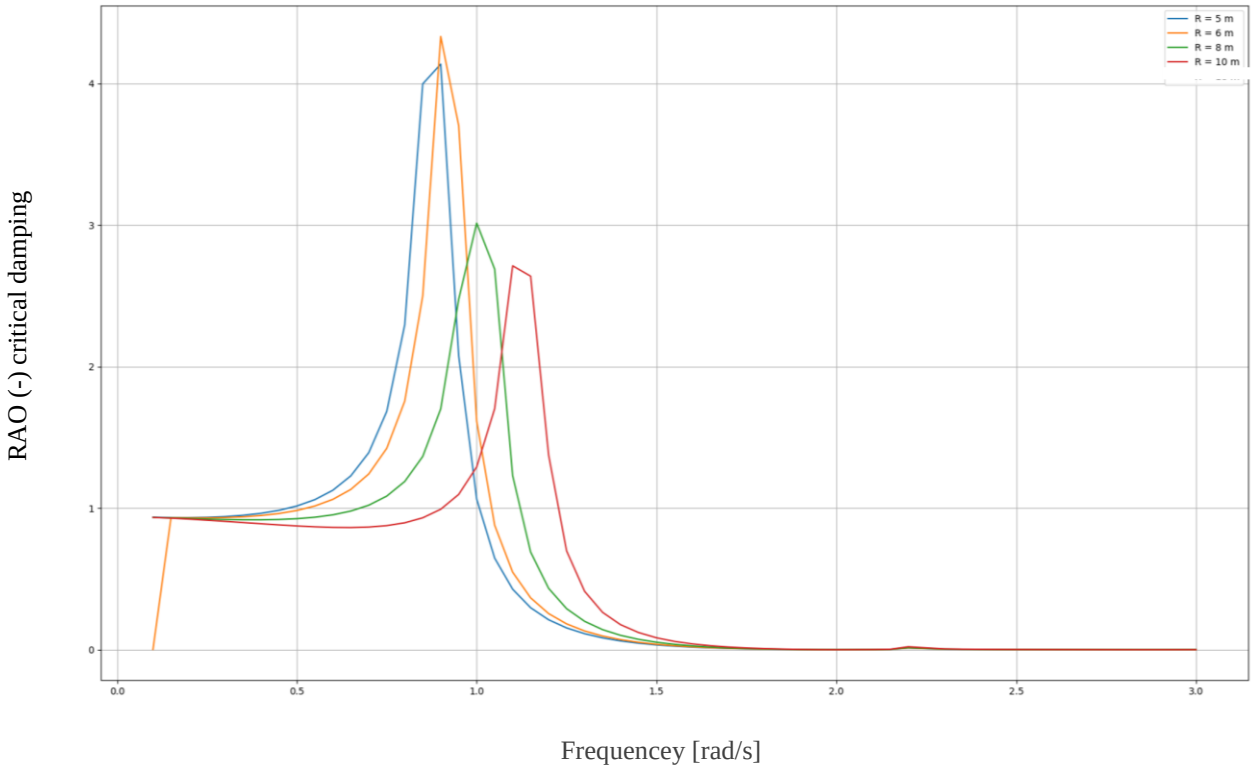

Figure 29 - RAO for varying R without critical damping - bullet

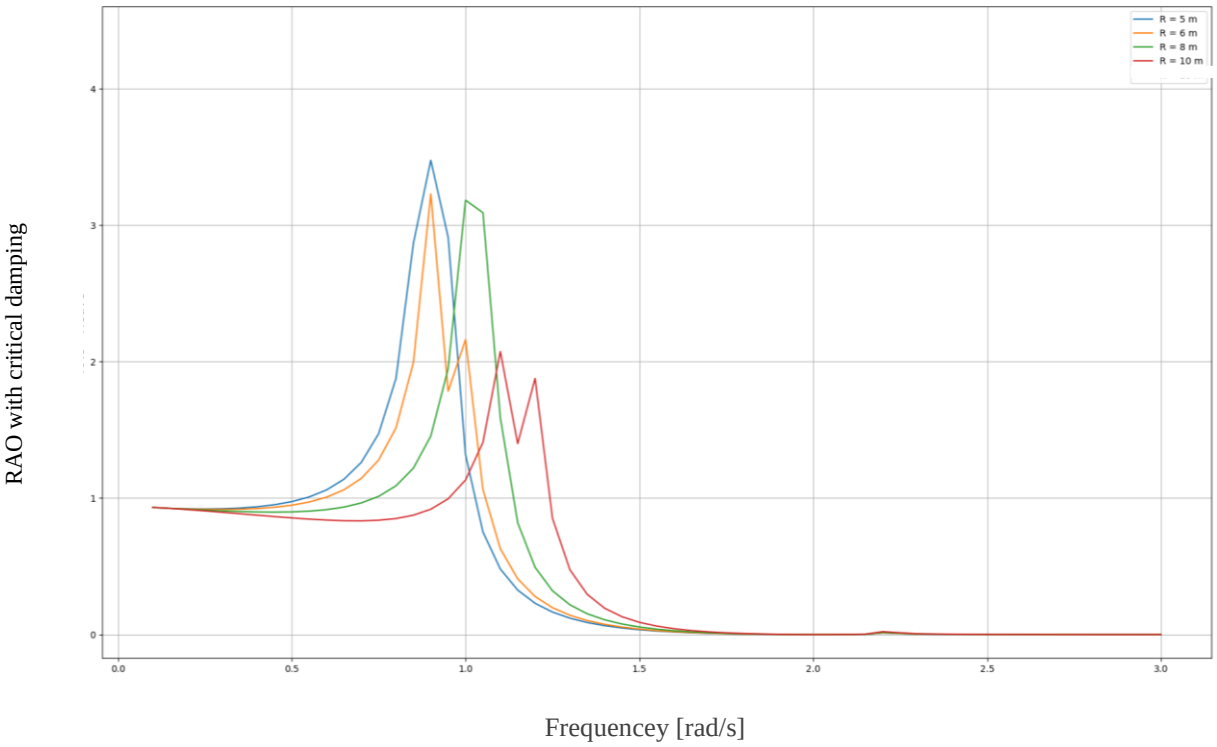

Figure 30 - RAO for varying R with critical damping

4.2 Results on the optimization

Moreover, the results from objective functions f1 and f2 are illustrated, varying the buoy's radius and the height of the buoy. Finally, the results on the constraints are presented for some geometries and compared to the unconstrained results.

Objective function 1, f1

This section will present the energy performance for the WEC, considering objective function f1, which is calculated using Eq. 43. The results are first presented as surface plots in 3-D for both sites and shapes. Further, each of the 3-D plots is given, seen from above, as 2-D plots. Figure 32-35 are illustrating the average annual energy absorption for the bullet for both sites

Further on, Figure 36-39 show the average yearly energy absorption for the cone for both sites. The results are calculated based on the sampling within the upper and lower boundaries for the shape's two design parameters, R and H. The white area indicates the most inadequate energy performance. The darker the blue color appears to be, the higher the energy performance.

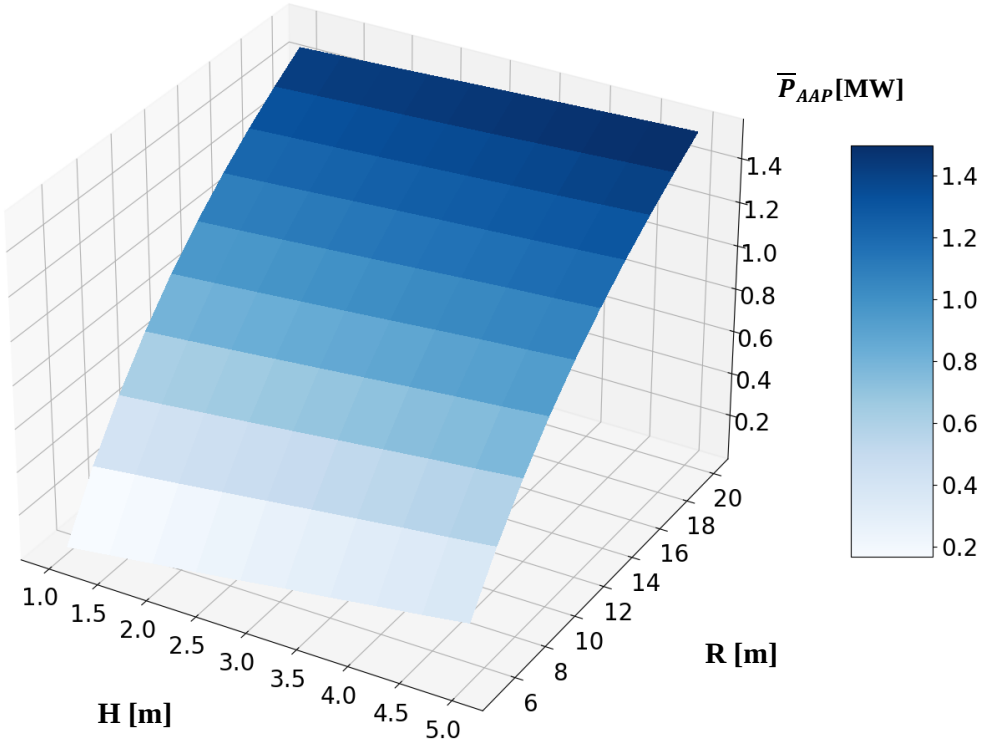

Figure 31 – 3-D plot of annually average power absorption for bullet (site 1)

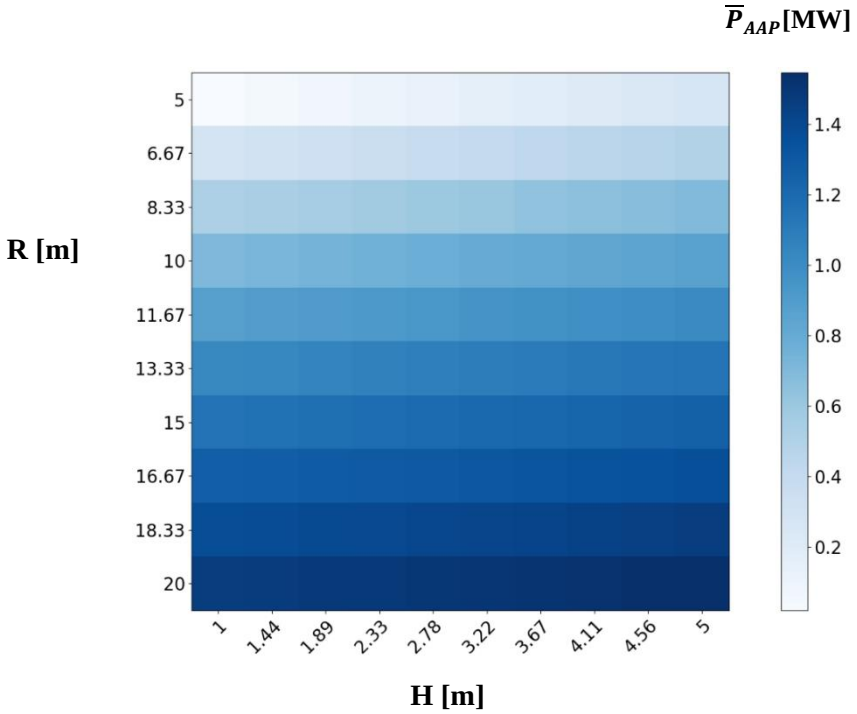

Figure 32 - 2-D plot of annually average power absorbtion for bullet (site 1)

The combination of high values for R and high values of H leads to increased power performance. The trend of the plot shows that to maximize the power production for each oscillation mode, the WEC should be built as large as possible. However, the radius of the floater is the dominant effect on the power absorption properties of the WEC in heave motion compared to height. As expected, the highest average annual absorbed power is found for the highest chosen value for the design parameters R and H. For both shapes, objective function 1 is maximized for R=20 meters and H=5 meters, whereas the annual energy performance for the bullet is approximately 1.55 MW at site 1. See Figure 43. At site 2, the peak corresponds to about 1.80 MW which can be seen in Figure 34. The results correspond to (Babarit, Hals, et al. 2011), whereas the power increases with the buoy volume. The result indicates that site 2 corresponds to higher annual energy performance. Hence, this accounts for both the bullet and the cone. The cone has a yearly performance of 1.66 MW for site 1, illustrated in Figure 36. Further, Figure 40 show the result for site 2, the maximum energy output is 1.93 MW. Table 4 presents the results, whereas the objective function is maximized. The corresponding values for the second objective function are added in the same table.

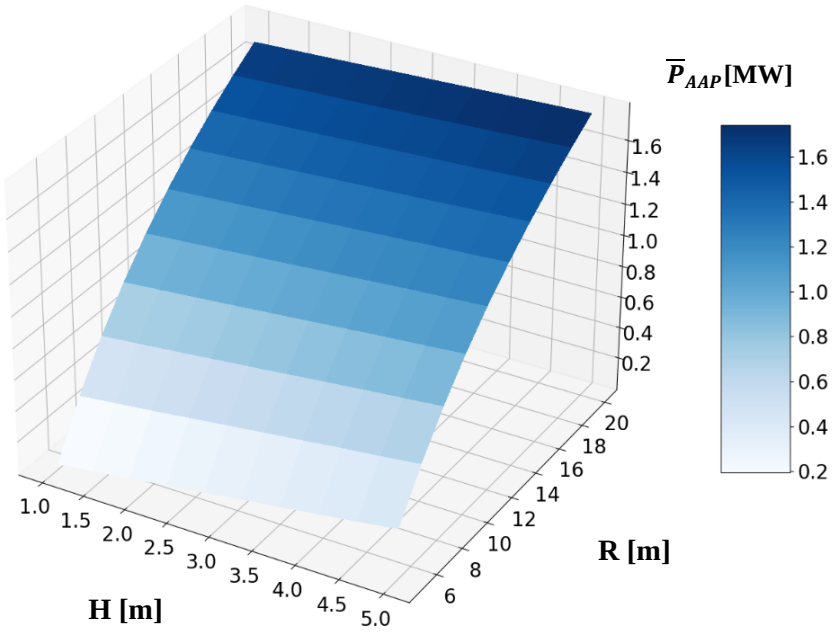

Figure 33 - 3-D plot of annually average power absorption for bullet (site 2)

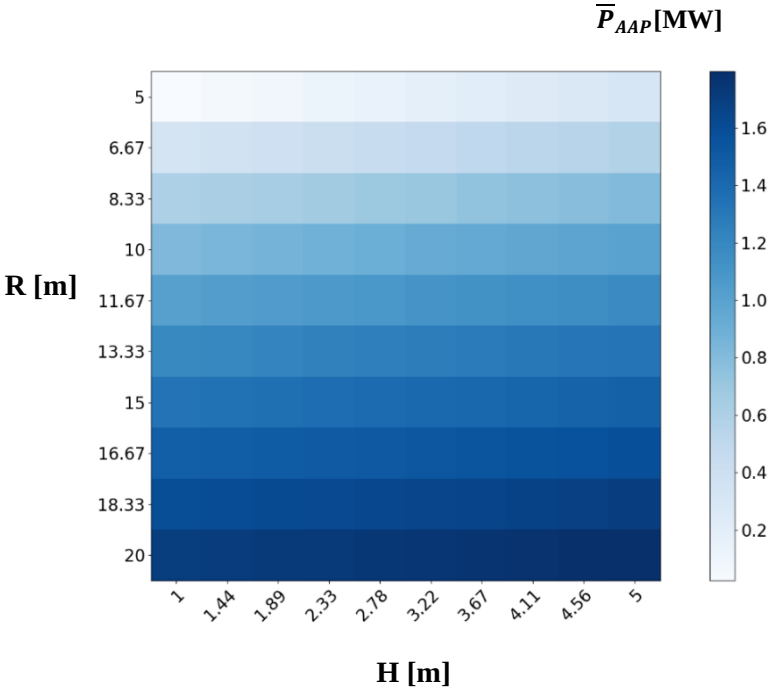

Figure 34 - 2-D plot of annually average power absorbtion for bullet (site 2)

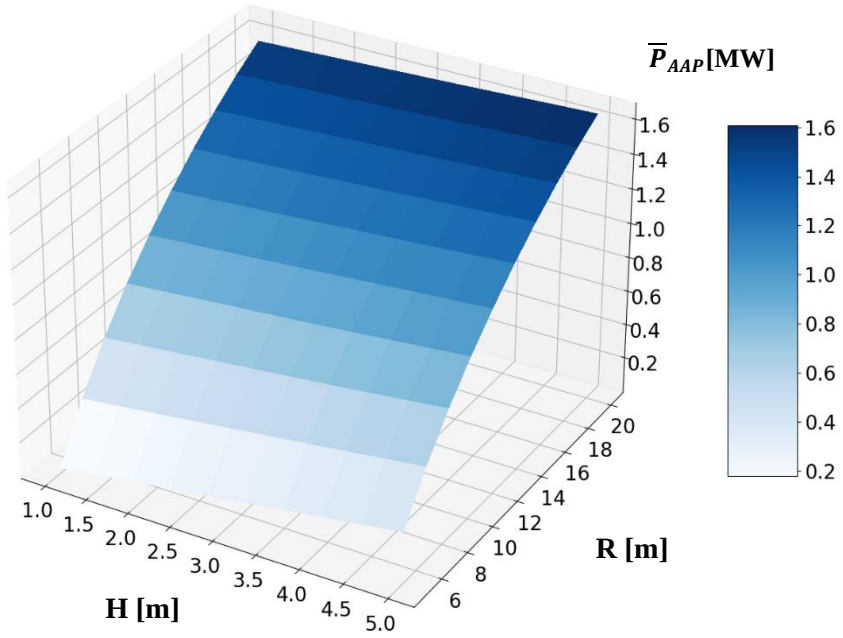

Figure 35 – 3-D plot of annually average power absorption for cone (site 1)

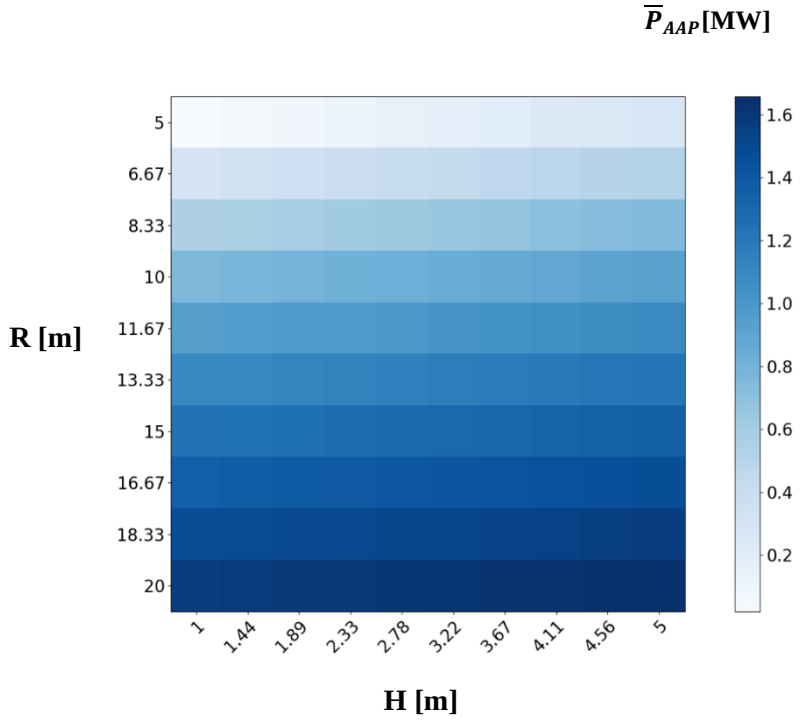

Figure 36 - 2-D plot of annually average power absorbtion for cone (site 1)

Even though an increased buoy increases the energy performance, it is essential to be aware that the growth rate of power decreases with increased volume. It is also necessary to include the aspect of cost. Thus, the second objective function, f2, is further applied to avoid over-dimensioning and make sure that the size of the buoy is cost-effective in terms of the annual absorbed energy and the mass of the floating structure.

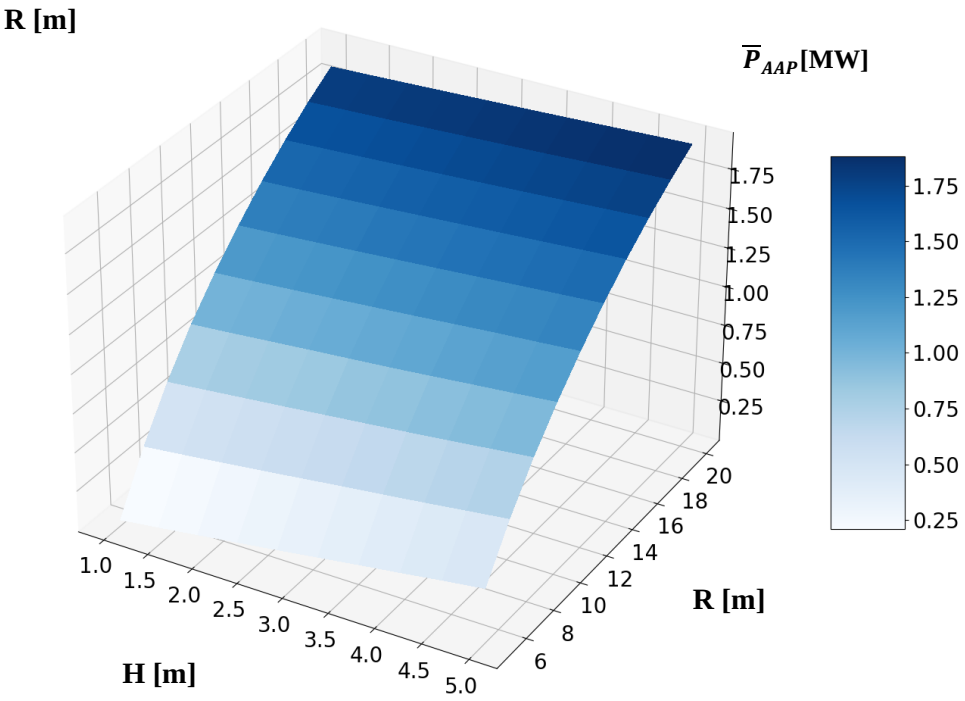

Figure 37 - 3-D plot of annually average power absorption for cone (site 2)

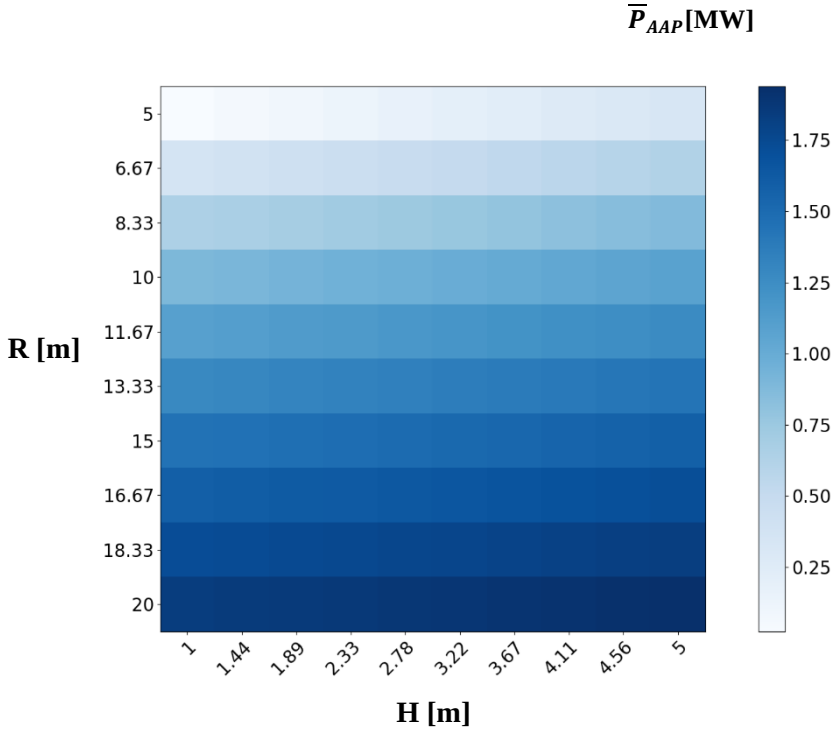

Figure 38 - 2-D plot of annualy average power absorbtion for cone (site 2)

To sum up, the figures display the average power production for the WEC as a function of its radius and height. The power increases with an increase in radius and height, as expected. On the other hand, a change in the radius is the main contributor to higher power output than height. The results are obtained assuming LWT. As a result, the hydrodynamic results are most likely not linear, and the power values can differ, even though the trend is expected to be the same.

Objective function 2, f2

Sensitivity analysis of the approximated LCoE values is presented in surface plots, similar to the power plots. The LCoE values are calculated using Eq. 46. Compared to objective function 1, the color bar is reversed for objective function 2. It is a consistent choice to keep the "best" result the darkest color. Thus, the white area indicates the most inadequate LCoE, while the darker the blue color appears to be, the lower cost per energy. Figure 39-42 illustrates the annual LCoE for the bullet in both sites. While, Figure 43-46 present the annual LCoE for the cone in both sites.

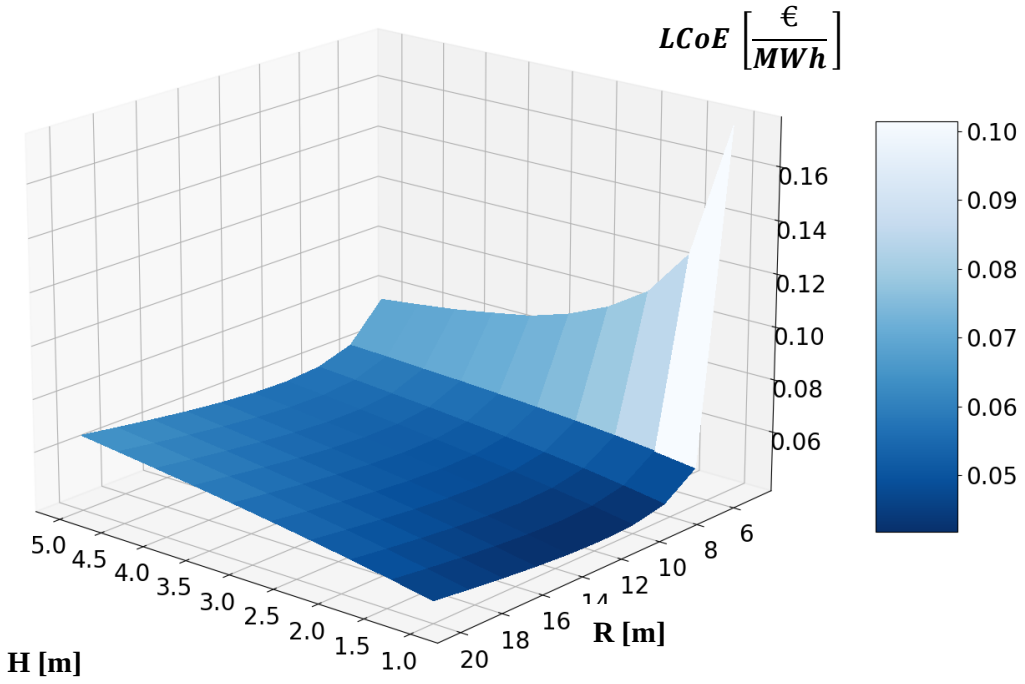

Figure 39 - 3-D plot of annually LCoE bullet (site 1)

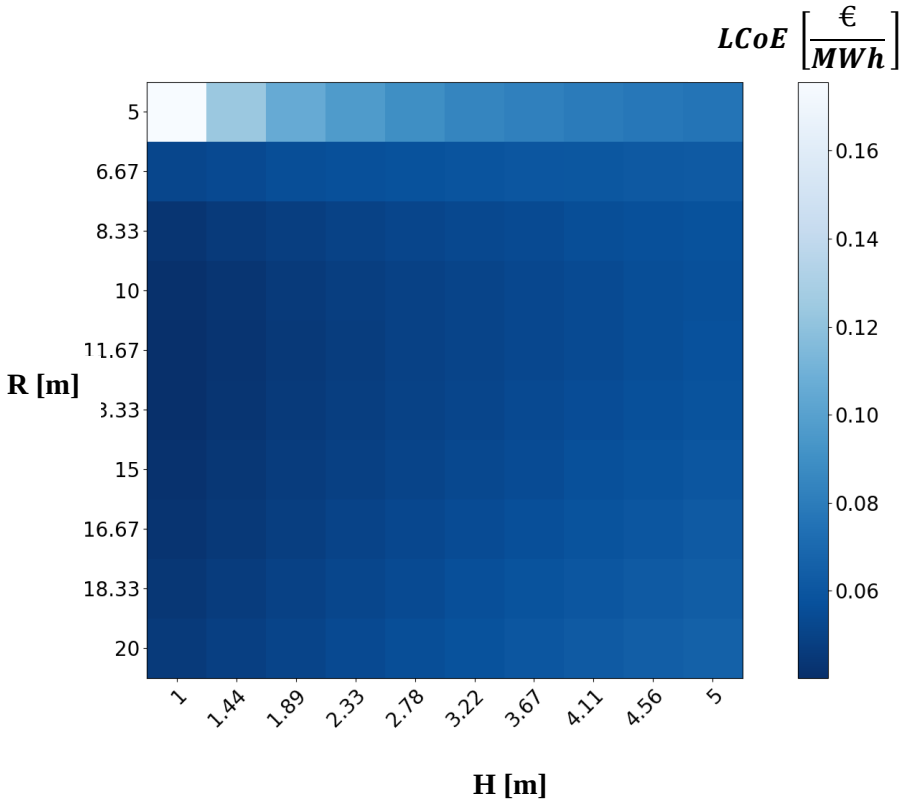

Figure 40 - 2-D plot of annually LCoE for bullet (site 1)

The cost per amount of energy will increase for minimal radius and height (small geometries). The minimum value for LCoE is achieved for a radius between 11 and 13 meters for both shapes, regardless of the structure's height. As for the buoy height (Sergiienko, Neshat et al. 2020), all optimization algorithms converged to the lowest assigned limit. This also accounts for the results in the present study. Hence, the buoy height should be limited to produce as cheap energy as possible without further constraints. The LCoE rate has a steep growth rate for small geometries compared to larger geometries. The height has a significant effect on the negative development of LCoE, especially for floaters of low radius.

Figure 40 illustrates the LCoE value for the bullet for site 1. The minimized cost is about 0.0040 €/MWh. Since the energy production is a bit higher for site 2 the corresponding value represent a cost at about 0.0037 €/MWh. See Figure 43.

Further, the LCoE is calculated for the cone at site 1 which is displayed in Figure 44. The lowest cost is approxiamately at 0.0039 €/MWh. The LCoE for the cone at site 2 is presented in Figure 46. The cone for site 2 has the highest energy output, and therefore the lowest LCoE at approximately 0.0027 €/MWh.Even though it is hard to draw any conclusion from the specific offshore site, shape, or geometry, it is possible to see a common trend for a cost-effective design of the WEC.

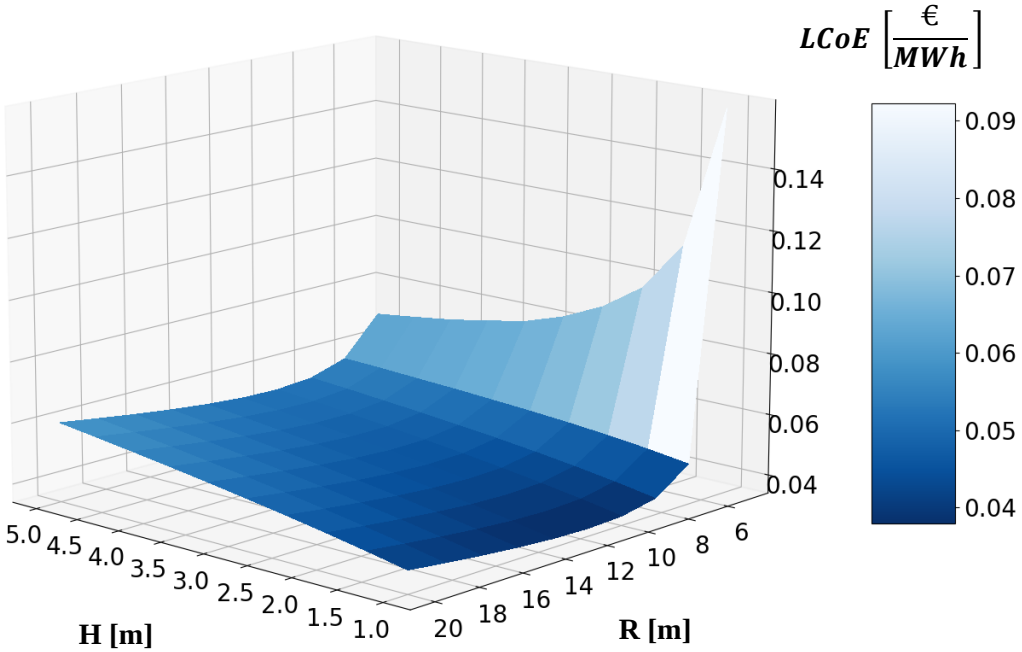

Figure 41 - 3-D plot of annually LCoE for bullet (site 2)

According to (Sergiienko, Neshat et al. 2020) expensive and accurate CFD simulations analysis

of potential power production and reliable model estimation of the LCoE value resulted in an optimized design for a WEC system in Australia at a 12.5 m radius. The research substantiates the findings in the present study. Table 5 present the results, whereas objective function 2 is minimized. The corresponding value for f1 is shown in the same table.

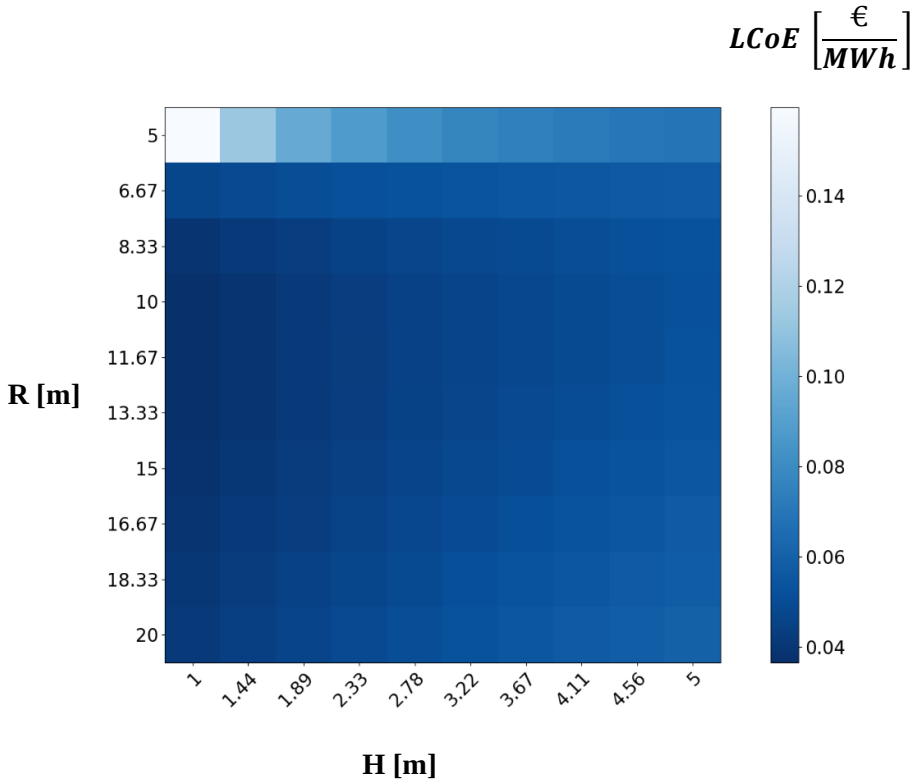

Figure 42 - 3-D plot of annually LCoE for bullet (site 2)

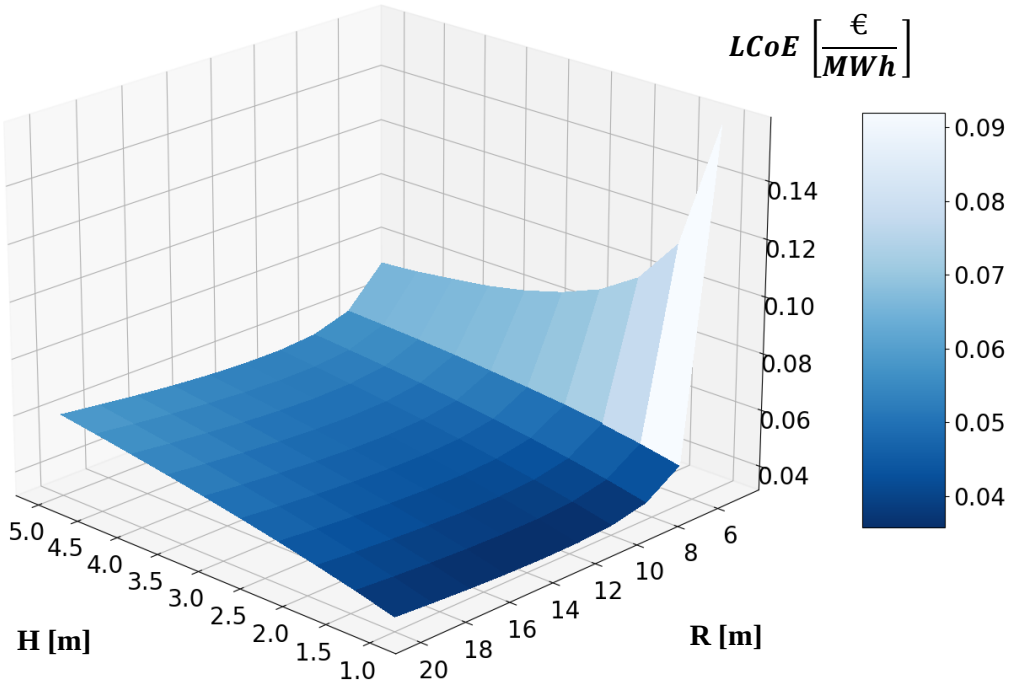

Figure 43 - 3-D plot of annually LCoE for cone (site 1)

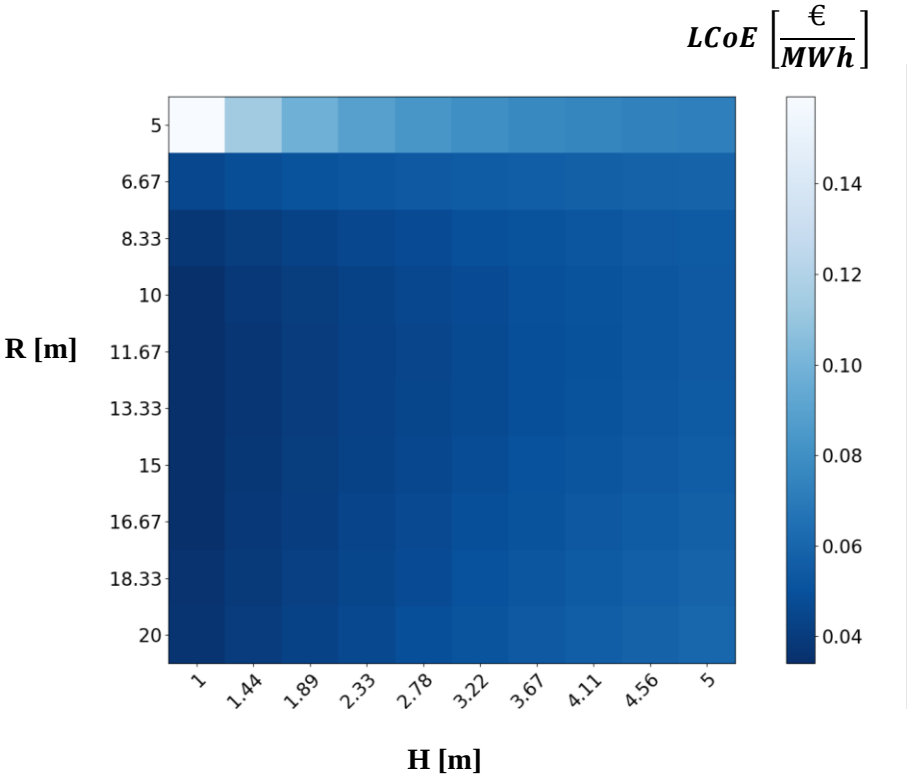

Figure 45 - 2-D plot of annually LCoE for cone (site 1)

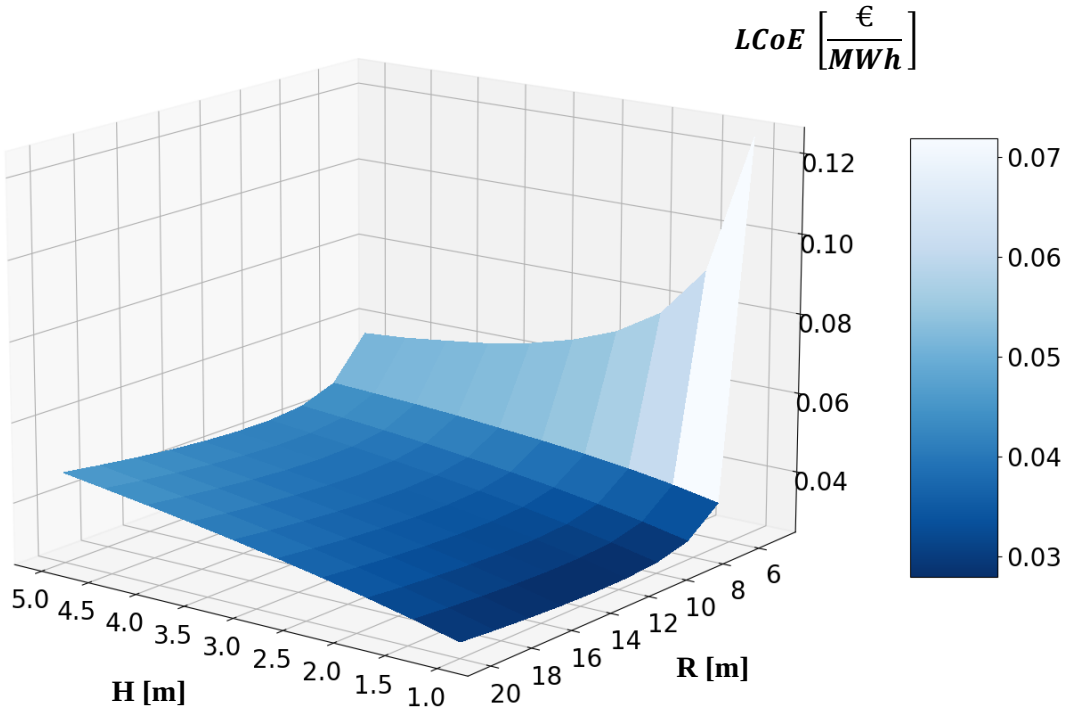

Figure 44 - 3-D plot of annually LCoE for cone (site 2)

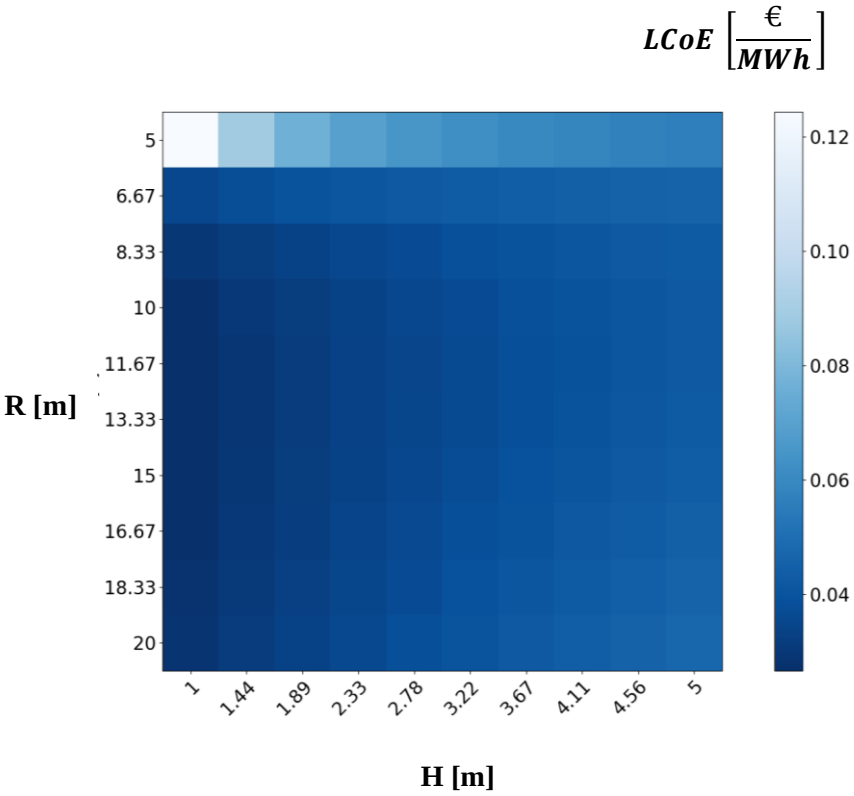

Table 4 - Results for R, H, f1, f2 when maximizing objective function 1

	Bullet		**Cone**	
	Site 1	Site 2	Site 1	Site 2
R [m]	20.0	20.0	20.0	20.0
H [m]	5.0	5.0	5.0	5.0
f1 [MW]	1.55	1.79	1.65	1.93
f2 [price/kwh)	0.066	0.057	0.060	0.047

Table 5 - Results for R, H, f1, f2 when objective function 2 is minimized

	Bullet		**Cone**	
	Site 1	Site 2	Site 1	Site 2
R [m]	11.3	11.3	11.3	11.3
H [m]	5.0	5.0	5.0	5.0
f2 [price/kwh]	0.040	0.036	0.039	0.027
f1 [MW]	1.02	1.19	1.13	1.28

4.3 Results on the constraints

Stability

To ensure the stability of the floating structure, a physical constraint to ensure stability has been applied. The stability of the floating body is plotted in Figure 47 and Figure 48 and is calculated using Eq. 47. The floating body is assumed to be stable for values of GM lower than 1. It accounts for most R and H combinations for the design boundaries, except for buoys of low radius and high values of height. The stability constraint will not directly influence the result of a feasible design for the WEC: Based on the sensitivity analysis from 4.2, neither objective function reaches values near maximum or minimum for unstable buoys.

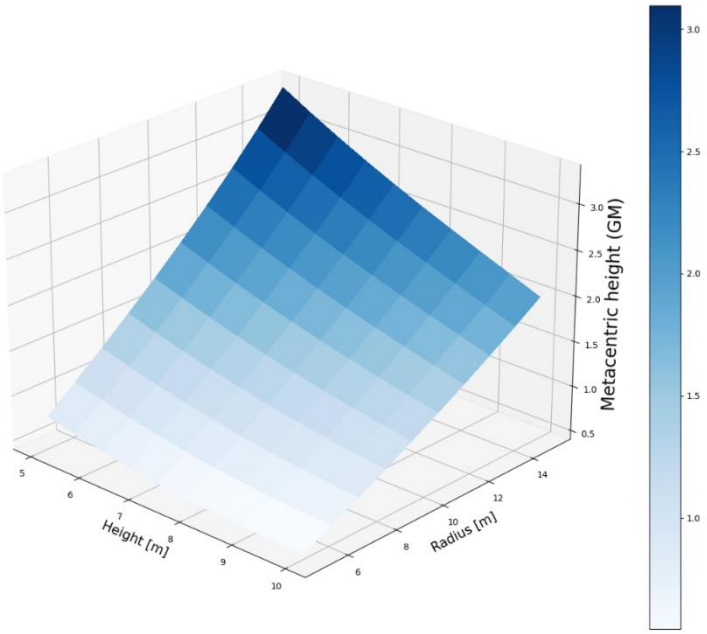

Figure 47 - Metacentric height (GM) of bullet

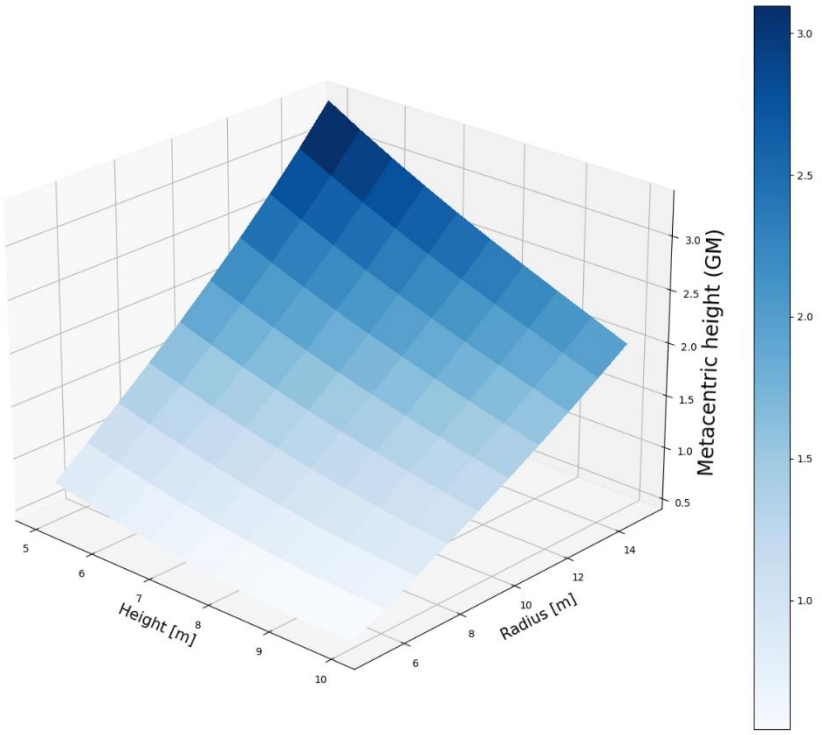

Figure 48 - Metacentric height (GM) of cone

Heave motion restriction

The analysis for the stroke restriction is applied in the following section. The results of the constraint will indicate the amplitude in heave motion that is probable to be exceeded every 3 hours. Calculations are performed for each sea state to see how the constraint affects the annual absorbed power. Furthermore, the constraint is employed on the power output for both sites to compare the affection of the absorbed power. Among all genereated geometries the following design of the shapes is presented; **(1)** R = 11 m, H = 1 m, **(2)** R = 13 m, H = 1 m, **(3)** R = 11 m, H = 2 m and **(4)** R = 13 m, H = 2 m. These geometries have properties that satisfy a combination of high energy production and low cost in addition to achieve high energy production for the heave motion restriction. Once the value for $\tilde{X}3h$ exceeds the set limit value, the WEC will stop its production in the corresponding sea state. The limit is based on the geometry of the bouy, whereas the maximum value can not exceed a value higher than two times the cylindrical height, 2H. It means that the $\tilde{X}3h$ value can not exceed 2.0 m and 3.0 m, respectively.

The restriction is more likely to be exceeded for the smaller diameter. Therefore, the graphs of geometries of R = 11 m reach higher values of the largest crest height. Further, an increase in height results in a lower $\tilde{X}3h$ value relative to its height. Sea states of periods 6.0 s and 7.0 s have the highest contribution to the crest height, whereas the most energetic waves, Hs = 3.5 m, and Hs = 4.5 m, are more likely to cause higher heave motion.

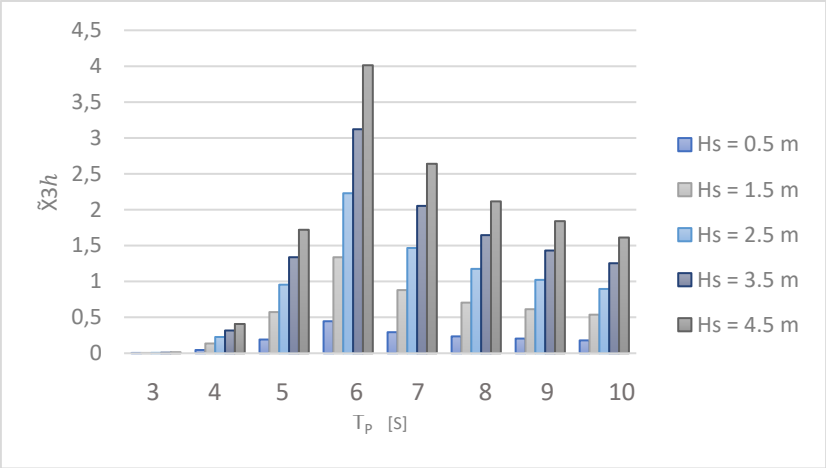

Figure 49 - Heave motion, $\tilde{X}3h$ for R = 11 m, H= 1 m, TD = 12 m (cone)

Figure 49 shows the result for heave motion for **(1).** The heave motion exceeds the limit of 2.0 m for six different sea states and will have a noticeable effect on reducing power absorption. The red line in the figure marks the maximum value. Hence, the exceedance account of values of Tp = 6 and 7 s and Hs =3.5 and 4.5 m.

Figure 50 present the result for heave motion for **(2)**. The heave motion exceeds the limit for three sea states and will affect the average power absorption.

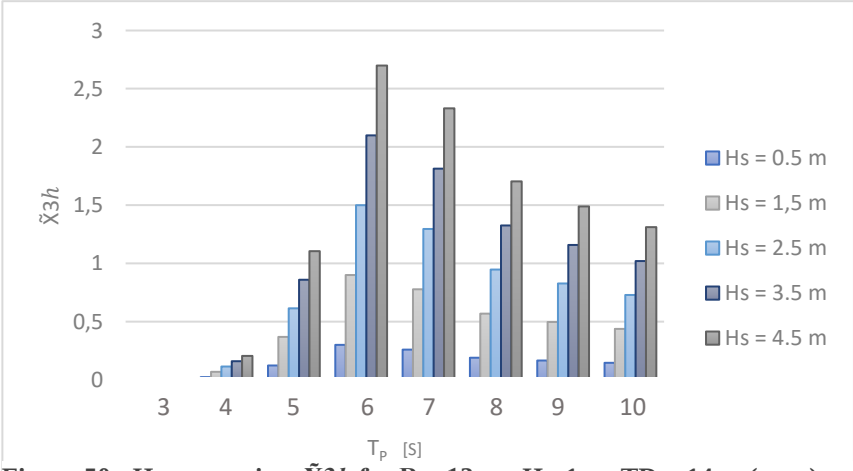

Figure 50 - Heave motion, $\tilde{X}3h$ for R = 13 m, H= 1 m, TD = 14 m (cone)

However, it is a great reduction of exceedance affected by increasing R of 2 m. The exceedance of 2 m happens at Tp = 6 s and 7 s and for Hs =3.5 and 4.5 m. The results indicate that the increase in radius limits the heave motion in general. Compared to Figure 49, the peak value is about 4 m while the following geometry peaks at around 2.7 m.

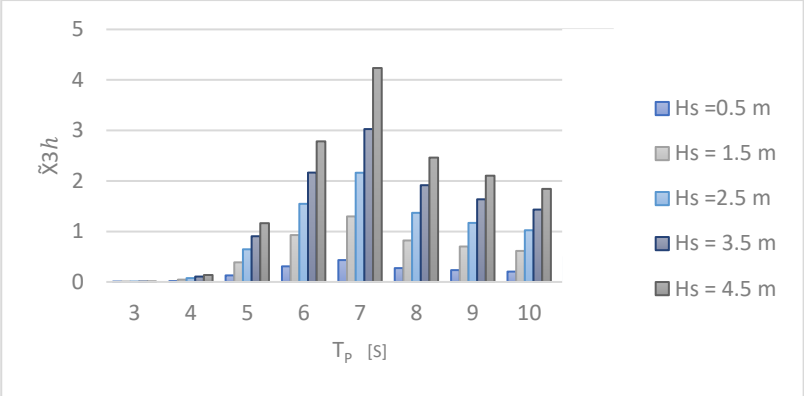

Figure 51 - Heave motion, X̃3*h* for R = 11 m, H= 2 m, TD = 13 m (cone)

A further result of the analysis will evaluate geometries with an increased cylindrical height. The results indicate that an increase in the radius will limit the heave motion rather than increase the figure's cylindrical height, H. The same trend accounts for (3) and (4) as for (1) and (2). The increase of R will lead to a rare exceedance of the motion limit. According to the limit, the geometry of R = 13 m and H = 2 m will exceed it for neither sea state. Figure 51 shows the heave motion for (3), and lastly, the heave motion for (4) is presented in Figure 52. The analysis is conducted for site 1 and site 2. An interesting finding is that the result differs entirely based on the specific site conditions. The density of waves is distributed differently for different locations.

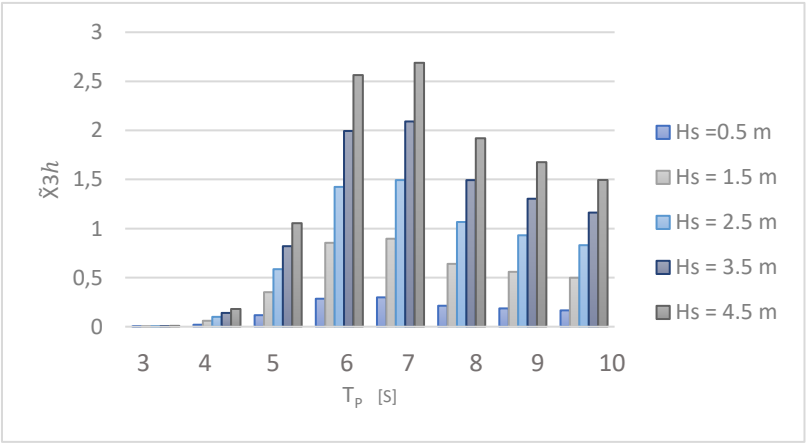

Figure 52 - Heave motion, X̃3*h* for R = 13 m, H= 2 m, TD = 15 m (cone)

The values of $\tilde{X}3h$ varies with the same trend as for the cone. The results are presented in smaller diagrams below, from Figure 54-56. After applying the constraint is seem like the cone still achieve the highest energy output.

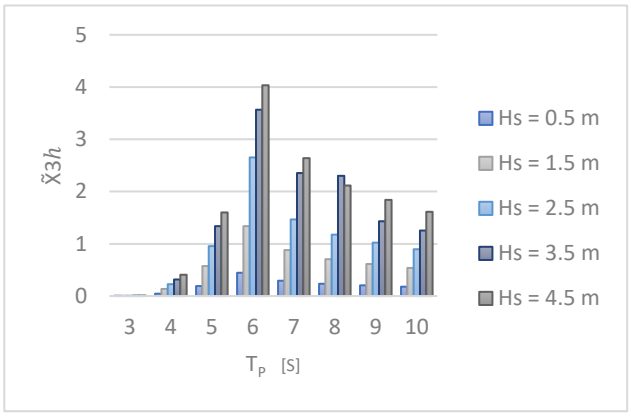

Figure 56 - Heave motion, $\tilde{X}3h$ for R = 11 m, H= 1 m, TD = 12 m (bullet)

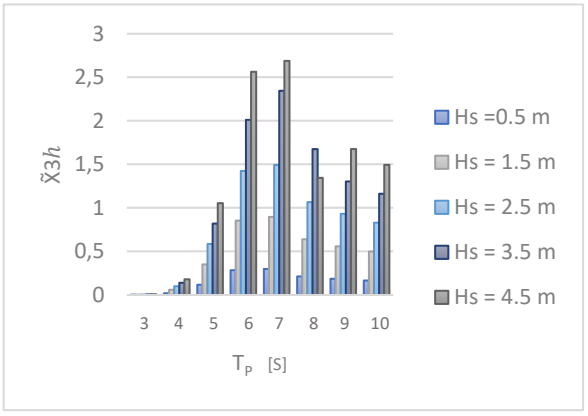

Figure 53 - Heave motion, $\tilde{X}3h$ for R = 13 m, H= 1 m, TD = 14 m (bullet)

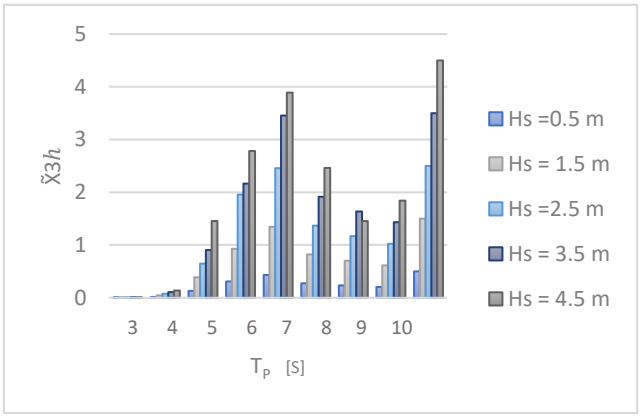

Figure 54 - Heave motion, $\tilde{X}3h$ for R = 11 m, H= 2 m, TD = 13m (bullet)

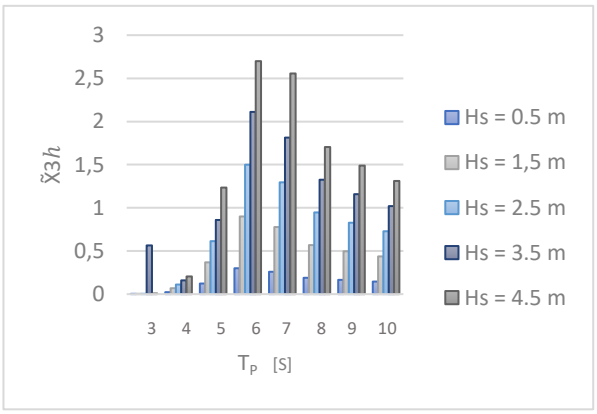

Figure 55 - Heave motion, $\tilde{X}3h$ for R = 13 m, H= 2 m, TD = 15 m (bullet)

Finally, Table 6-10 shows how the constraint of a motion restriction affects the annual average power absorption. Table 6 includes the power output before and after applying the heave motion constraint. The column to the very left, called “Difference” calculates the percentage of decrease in energy performance.To conclude, geometries with R = 13 m and H = 2 m can be a feasible design based on the result of the present study. It is a large buoy, which means that the energy output is high. The price per amount of energy is near to a minimze in addition to fulfill the applied constriants.

Table 6 - Comparison for unconstrained and constrained result site 1 (cone)

	Annual average power absorption [MW]				**Difference**	
	Unconstrained result		Constrained result		%(-)	
$H_{[m]}$ / $R_{[m]}$	1	2	1	2	1	2
11	1,130	1,432	0,865	1,065	**22 %**	**14 %**
13	1,342	1,398	1,075	1,342	**20 %**	**0 %**

Table 7 - Comparison for unconstrained and constrained result site 2 (cone)

	Annual average power absorption [MW]				**Difference**	
	Unconstrained result		Constrained result		%	
$H_{[m]}$ / $R_{[m]}$	1	2	1	2	1	2
11	1,280	1,321	1,083	1,234	**15 %**	**7 %**
13	1,336	1,425	1,167	1,425	**13 %**	**0 %**

Table 8 - Comparison for unconstrained and constrained result site 1 (bullet)

	Annual average power absorption [MW]				**Difference**	
	Unconstrained result		Constrained result		%	
$H_{[m]}$ / $R_{[m]}$	1	2	1	2	1	2
11	1,02	1,124	0,786	0,956	**23 %**	**15 %**
13	1,234	1,375	1,012	1,234	**18 %**	**0 %**

Table 9 - Comparison for unconstrained and constrained result site 2 (bullet)

	Annual average power absorption [MW]				**Difference**	
	Unconstrained result		Constrained result		%	
$H_{[m]}$ / $R_{[m]}$	1	2	1	2	1	2
11	1,19	1,245	1,032	1,167	**13 %**	**6 %**
13	1,204	1,385	1,087	1,385	**10 %**	**0 %**

The result for site 1 and 2 appears to be diffferent caused by the density of the waves. To present the difference, a competative study will be done in the next section.

4.4 Comperative study for site 1 and site 2

The following section will compare how the annual average absorbed power is distributed for 40 different sea states, considering site 1 and site 2. For the analysis, the results are considered for one design of the bullet and the cone, both with design parameters equal to R = 13 m and H = 1 m. Based on the results from 4.2 and 4.3 these parameters represent a decent model for a WEC. The results are presented in Figure 57 -59 which displays a heat plot for each geometry and site. All heat plots represent objective function 1 for one specific geometry (R=13 m, H=1 m). The x-axis includes the T_p values, while the y-axis contains the H_s values. The heatmap makes up a 5x8 plot with the corresponding energy performance for each specific sea state.

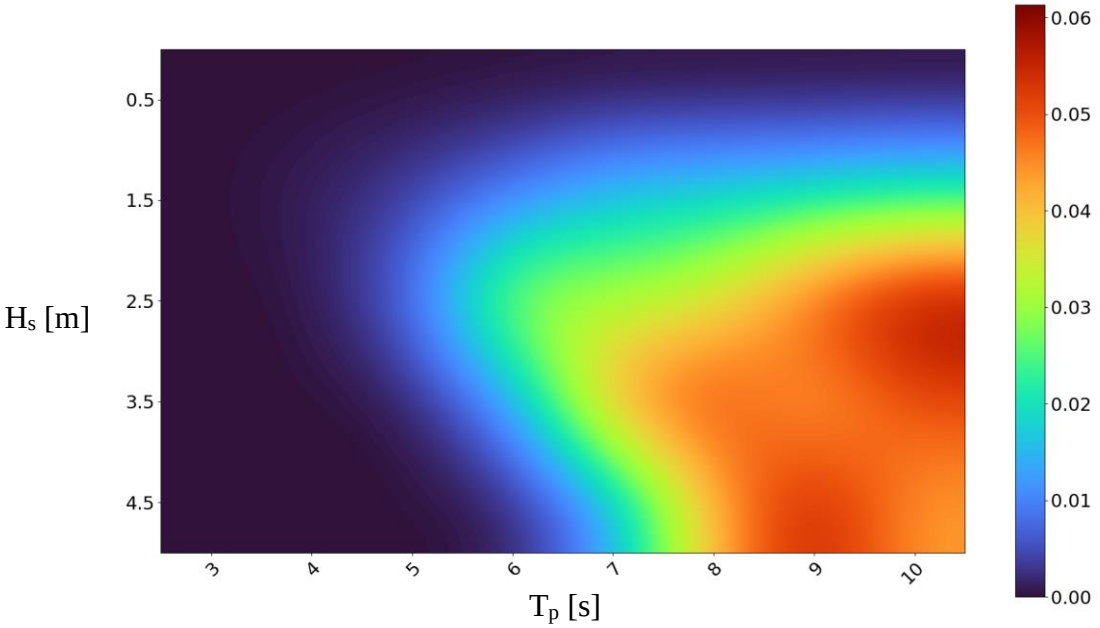

Figure 57 - Annually energy distrubution for 40 sea states for bullet (site 1)

Site 1 has a high density of waves that consist of high period waves compared to site 2. Most of the total power output for the bullet is centered around these areas. The distrubtion is plotted in Figure 57. The most favorable sea states for the bullet are **(1)** H_s=2.5 m, T_p=10.5 s, and **(2)** H_s=4.5 m, T_p=9.5 s. In general, sea states with Tp higher than 7.5 and Hs bigger than 2.5 contribute significantly to the bullet's overall energy performance. This could be beneficial, whereas the site includes a high occurrence of waves that are considered very energetic.

The energy distribution is further plotted for site 1 for the Cone shape. Figure 58 displays that the most energy comes from waves of high T_p values, similar to the bullet. However, the cone seems to have a more dominant effect from waves with a lower significant wave height. The energy density is more concentrated around a smaller range of sea states. 68 % of the power output is comes from the following sea states, **(1)** H_s = 1.5 m and T_p = 10.5 s, **(2)** H_s = 2.5 m and T_p=10.5 s, and **(3)** H_s = 1.5 m and T_p = 9.5 s.

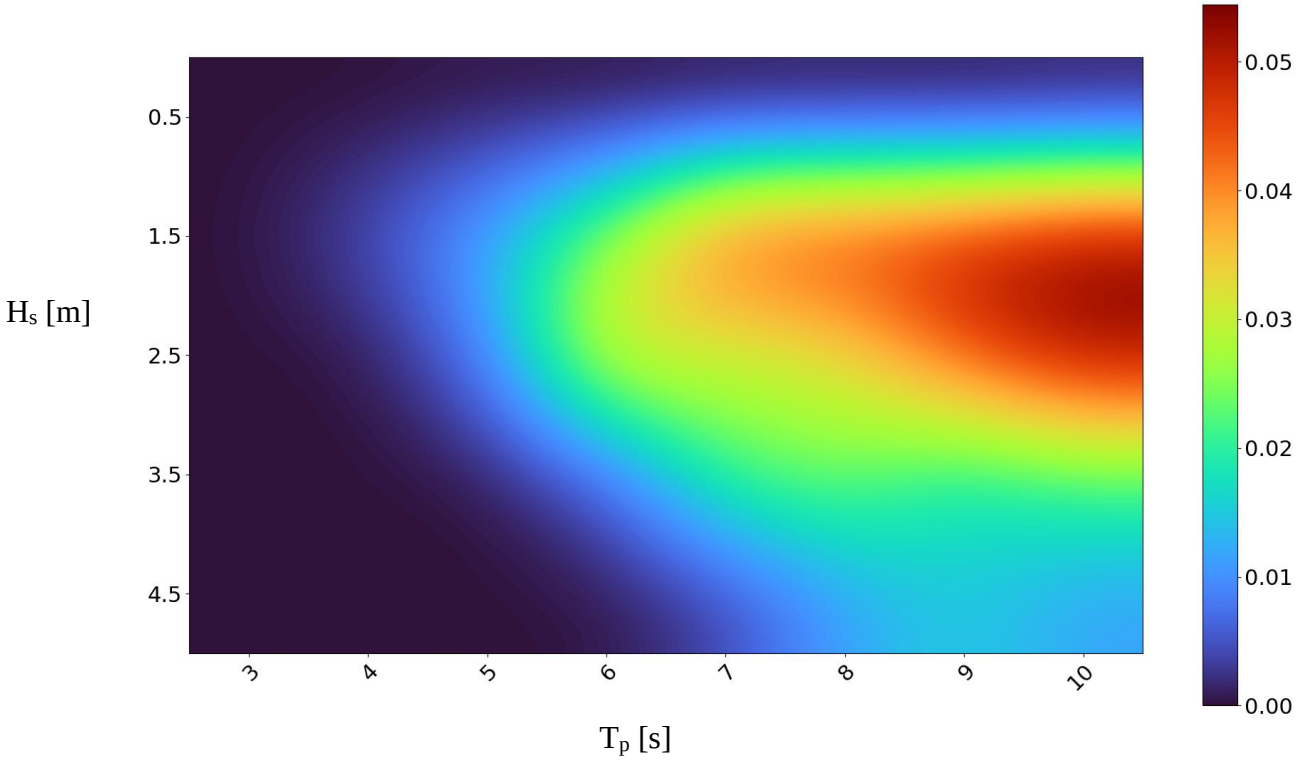

Figure 58 - Annually average energy distrubution for 40 sea states for cone (site 1)

Whereas site 1 has a high density of waves that consist of waves of high periods, site 2 has a higher density of T_p values ranging in the lower area. In Figure 59, the heat plot displays how the power output is distributed for the bullet for site 2. Since the occurrence of sea states are higher for a lower period and lower wave height, it is expected that the energy distribution is maximized for other sea states compared to site 1. The energy output is also even more concentrated for this case, with most of the energy output dominated by two sea states, **(1)** H_s = 1.5 m and T_p = 5.5 s and **(2)** H_s= 1.5 m and T_p = 6.5 s. Even though the overall energy performance is higher for site 2 than site 1, site 2 has a higher occurrence of waves that are considered more energetic.

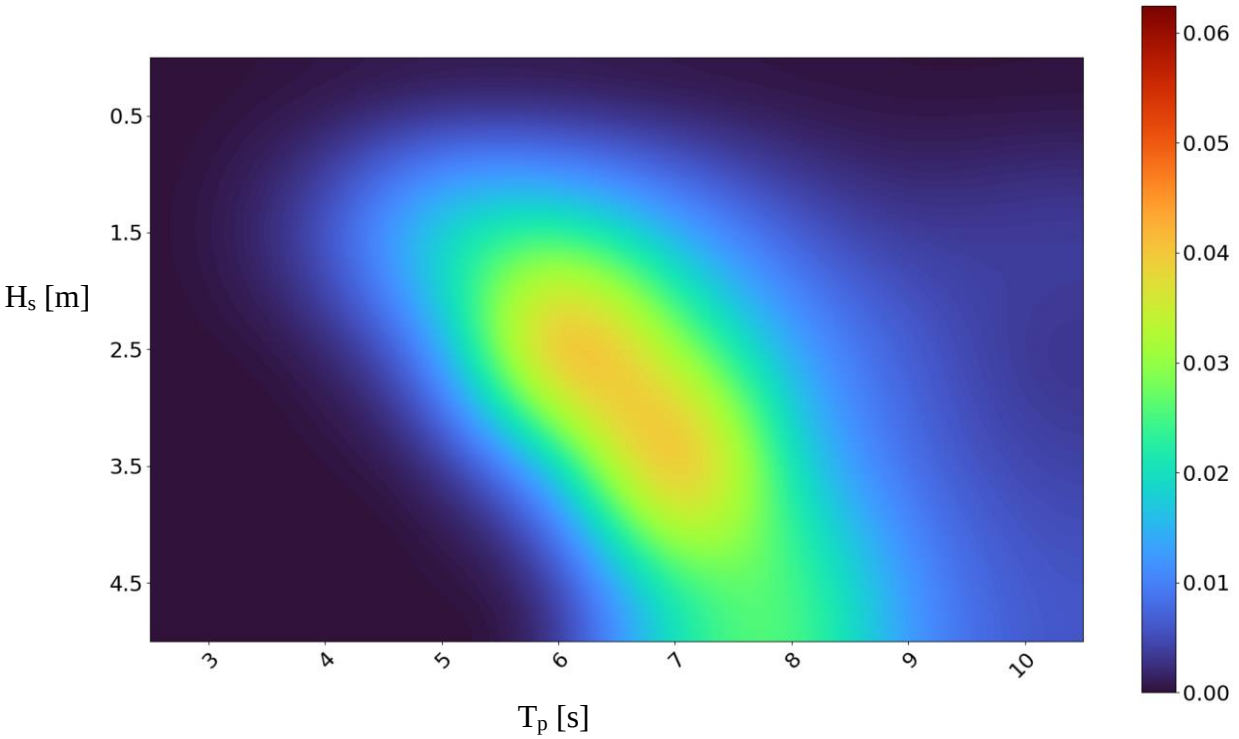

Figure 59 - Annually average energy distribution for 40 sea states for bullet (site 2)

At last, the heatmap is presented for the cone at site 2 in Figure 60. The energy is distributed quite similarly to the bullet for the same site. However, the cone for the site is more affected for sea states ranging in waves with higher significant wave height and higher period. The most dominant sea states for the cone in site 2 are the following, **(1)** Hs= 2.5 m and Tp = 6.5 s.

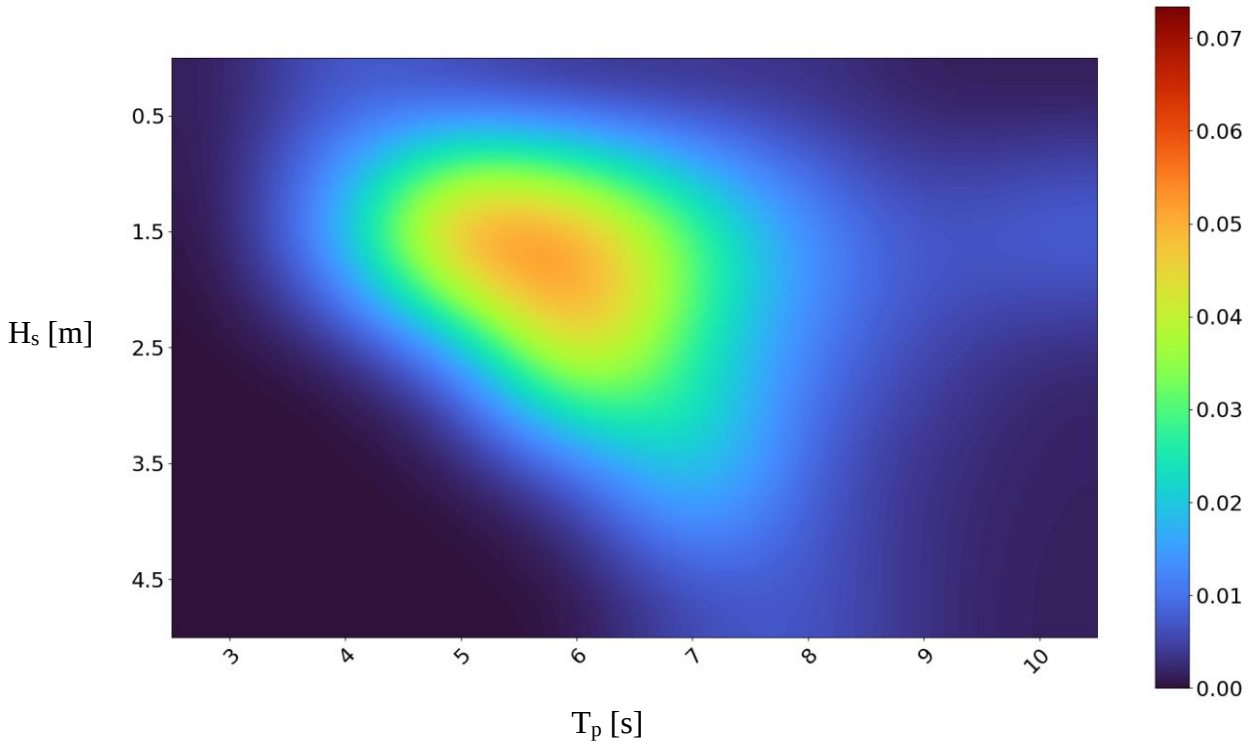

Figure 60 - Annually average energy distribution for 40 sea states for cone (site 2)

As for all 40 sea states, low range sea states (H_s < 2.5 m and T_p < 7.5 s) represent relatively small waves. Hence, these waves can be regarded as the minimum threshold to produce electricity and are considered less energetic waves. Further on, the following selection of sea states with a significant wave height of at least 2.5 m and higher periods are deemed to have a high probability of occurrence. Hence, it is these areas that often are in focus by developers in the planning phase. These are more energetic waves and can have a significant contribution to the overall energy performance. Based on the result, it can be possible that site 1 is considered more feasible for developing WEC farms, even though the calculations show a higher total energy output for site 2. Site 1 has an increased occurrence of the most energetic sea state. In these sea states, the WECs are still in condition to operate. However, point absorber devices generally stop producing electricity in harsh weather conditions and switch to a safety mode. In this way, the floaters are protected against bottom slamming or breaking wave slamming.

5 Conclusion and future work

By employing LWT for a frequency domain model, the behavior of a heaving point absorber WEC is simulated. The open-source programs Nemoh and Salome are applied for the hydrodynamic computation. A cone and bullet-shaped buoy are evaluated, both with a cylindrical upper part. Ten different waterline diameters (between 5 m and 20 m) and ten various heights of the cylindrical part (between 5 and 10 meters) are considered to obtain the mesh grid for the calculations. Two constraints were introduced in the present study: a constraint to ensure stability and a heave motion constraint.

According to objective function 1 the buoy should be designed as large as possible (R=20 m, H=5 m, TD = 25 m). By the findings, the cone shape has an improved power performance compared to the bullet, whereas the average annual power absorption is approximately 1.93 MW. Whereas the selected drafts seemed to limitedly influence the power absorption, changing the diameter significantly affects the absorbed power.

Furthermore, by including the cost aspect as design criteria, the buoy should be built with a radius of 11-13 meters and a height as low as possible. Hence, the lowest cost per MWh for the buoy of both shapes is for R = 11 m and H = 1 m (TD = 12 m). The heave motion restriction had an affect on the annual average power performance in most cases. By increasing the radius of the bouy the motion decreased relative to its height. The conlcusion based on the results for applied constraints are to design a geometry of R = 13 m and H = 2.

Note that, in the preliminary numerical approach of the present study, optimal converter coefficients were determined. Thus, LWT neglects viscous effects such as vortex shedding. As a result, it can significantly impact the prediction of power absorption, which causes inaccurate results for high amplitude waves and steep waves. Nevertheless, even though the result may be somewhat inaccuratce, the calculations predict a trend that is excpected compared to relevant research.

The intergrated optimization process that are created for the automated connection for the open-soruce programs can allow for further and more accurate problem solving of the optimization work. It would include to apply an advanced method for the optimization problem such as gradient-based method, genetic algorithm or surrogate models.

Aderinto, T. and H. Li (2018). "Ocean wave energy converters: Status and challenges." Energies **11**(5): 1250.

J.D. Anderson. Computational Fluid Dynamics: The Basics with Applications, 1995.

Antonio, F. d. O. J. R. and s. e. reviews (2010). "Wave energy utilization: A review of the technologies." **14**(3): 899-918.

Bergdahl, L. (2009). Wave-induced loads and ship motions, Chalmers University of Technology.

Biran, A. and R. L. Pulido (2013). Ship hydrostatics and stability, Butterworth-Heinemann.

de Andres, A., et al. (2016). On the Optimum Sizing of a Real WEC From a Techno-Economic Perspective. International Conference on Offshore Mechanics and Arctic Engineering, American Society of Mechanical Engineers.

De Backer, G. J. D. o. C. E., Ghent University: Ghent, Belgium (2009). "Hydrodynamic design optimization of wave energy converters consisting of heaving point absorbers."

Drew, B., et al. (2009). "A review of wave energy converter technology." **223**(8): 887-902.

Evans, D. (1981). "Power from water waves." Annual review of Fluid mechanics **13**(1): 157-187.

Faizal, M., et al. (2014). "A design outline for floating point absorber wave energy converters." Advances in Mechanical Engineering **6**: 846097.

Gunn, K. and C. Stock-Williams (2012). Quantifying the potential global market for wave power. Proceedings of the 4th International Conference on Ocean Engineering (ICOE 2012).

Gunn, K. and C. J. R. E. Stock-Williams (2012). "Quantifying the global wave power resource." **44**: 296-304.

Hansen, R. H., et al. (2011). Model based design of efficient power take-off systems for wave energy converters. Proceedings of the 12th Scandinavian International Conference on Fluid Power, Tampere, Finland.

Hasselmann, K., et al. (1973). "Measurements of wind-wave growth and swell decay during the Joint North Sea Wave Project (JONSWAP)." Ergänzungsheft 8-12.

IEA (2021), *Global Energy Review 2021*, IEA, Paris https://www.iea.org/reports/global-energy-rev

Journée, J. M. and J. Pinkster (1997). "Offshore hydromechanics." TUDelft, Faculty of Marine Technology, Ship Hydromechanics Laboratory, Report No. 1112-K, Lecture Notes.

Kalofotias, F. (2016). Study for the hull shape of a wave energy converter-point absorber; design optimization & modeling improvement, University of Twente.

P. K. Kundu, I.M. Cohen, and D. R. Dowling. Fluid Mechanics, volume 40. 2012. ISBN 9780123821003. doi: 10.1002/1521-3773(20010316)40:6¡9823::AIDANIE9823¿3.3.CO;2-C.

Li, L., et al. (2015). "Joint distribution of environmental condition at five european offshore sites for design of combined wind and wave energy devices." **137**(3).

Li, L., et al. (2019). "Design optimization of mooring system: an application to a vessel-shaped offshore fish farm." **197**: 109363.

Mueller, M., et al. (2001). "Electrical aspects of direct drive wave energy converters."

Pecher, A. and J. Peter Kofoed (2017). Handbook of ocean wave energy, Springer Nature.

Ricci, P., et al. (2011). "Control strategies for a wave energy converter connected to a hydraulic power take-off." **5**(3): 234-244.

SALOME. SALOME Webpage, 2016. URL http://www.salome-platform.org/.

Salter, S. H. J. N. (1974). "Wave power." **249**(5459): 720-724.

Sergiienko, N. Y., et al. (2020). Design optimisation of a multi-mode wave energy converter. ASME 2020 39th International Conference on Ocean, Offshore and Arctic Engineering, American Society of Mechanical Engineers Digital Collection.

Thomas, G. J. O. w. e. (2008). "The theory behind the conversion of ocean wave energy: a review." 41-91.

Vantorre, M., et al. (2004). "Modelling of hydraulic performance and wave energy extraction by a point absorber in heave." **26**(1-2): 61-72.

Wahyudie, A., et al. (2015). "Robust and low computational cost controller for improving captured power in heaving wave energy converters." Renewable Energy **82**: 114-124.

Wellens, P. R. (2004). "Wave Energy–Study to determine the optimal performance of a floating wave energy converter." Delft University of Technology, Offshore Engineering, Student Thesis.

Zhou, B.-z., et al. (2020). "Motion response and energy conversion performance of a heaving point absorber wave energy converter." **8**.

Appendix A – Python coding

The following appendix will include a small selection of the coded python scripts. A brief description of each of the appendix is explained below.

Apendix A.1: Extract the results from Nemoh and store them as matrices for 6 DOF.

Appendix A.2: The following scripts is created for the derived RAO for all geometries

Appendix A.3: The following script is for the integrated optimization process. The scripts allows Salome and Nemoh to connect and to solve the optimization problem for a number of geometries and design paramters.

Appendix A.4: Includes the plot of JONWSAP spectrum

Appendix A.1

```
# -*- coding: utf-8 -*-
"""
Created on Mon Mar  8 15:32:50 2021

@author: Grete
"""



import numpy as np
import freqList from freq


def damping(i):
    with open('Results%d/RadiationCoefficients.tec' %i,  'r' ) as fil:
        DOF = 0                                 # DOF = degrees of freedom
        total = freqList
        listMatrix = list()
        arrayFreq = np.zeros(totalt)
        correction = 8                           # Skip the 8 first lines


        for i in range(freqlist*2):
            matrix = np.zeros((6, 6))
            listMatrix.append(matrix)

        # Goes through every line in  RadiationCoefficient file
        for lineIndex, line in enumerate(fil):

            index = (lineIndex - correction) % 60


            if lineIndex < 8:
                continue

            # Skips line
            if index == total:
                DOF += 1
                continue

            nAddedMass = 0  # Index for columns in Added Mass matrix
            nDamping = 0   # Index for columns in Damped matrix

            # Go trough every line of RadiationCoefficient file
            for i, element in enumerate(line.split()):

                # Add first column to freqlist
                if i == 0:
                    arrayFreq[index] = float(element)
                else:
                    # Add columns to Added Mass matrix (odd numbers)
                    if i % 2 == 1:
                        # Added mass
                        listMatrix[index][DOF][nAddedMass] = float(element)
                        nAM += 1
                    # Add columns to Damped matrix (even numbers)
                    else:
                        # Damping
                        listMatrix[index+total][DOF][nDamping] = float(element)
                        nD += 1
```

```
    listeAddedMass = list()
    listeDamping = list()


    listeAddedMass = listeMedMatriser[:totalt]


    listeDamped = listeMedMatriser[totalt:]



    return listeDamping, listeAddedMass
i=0
```

Appendix A.2

```
# -*- coding: utf-8 -*-
"""
Created on Tue Mar 23 14:30:34 2021

@author: Grete
"""


import matplotlib.pyplot as plt
import numpy as np
import cmath
import math as mt

from excitationforce import *
from addedmass import *
from damping import *
from phaseangle import *
from listfrequency import frequencies
from Constraint_master import *
from matrix import *
from variablesone import freq
from ptodamping import Bpto, Cspring
from masslist import Masslist

cmplxNumber=1j
variables=np.load('variablesMatrix.npy') #MSample for R and H
raoList=list()
num=100
numGeo=num*freq


for i in range(num):

    R=variables[i][0]
    H=variables[i][1]



    def RAO(R, H):

        # Manual Input
        massMatrix = np.zeros((59,6,6))       # MassMatrix 6x6 matrix
        for i in range(59):
            massMatrix[i] = matrix(R, H, t)

        springMatrix = np.zeros((59,6,6))     # SpringMatrix 6x6 matrix
        for i in range(59):
            springMatrix[i] = springmatrix(R, H, t)

        frequencyMatrix = np.zeros((59,1))             # FrequencyMatrix Scalar Value
        for i in range(freq):
            frequencyMatrix[i][0] = frequencies(i)[i]
        #frequencyMatrix.append(frequencyList[i][0])
        omega = frequencyMatrix

    # Nemoh Output

        addedmassMatrix = np.zeros ((59,6,6)) # AddedmassMatrix 6x6 matrix
        for i in range(59):
            addedmassMatrix[i] = AddedMass(k)[i]
```

```
    dampingMatrix = np.zeros((59,6,6))    # DampingMatrix 6x6 matrix
    for i in range(59):
        dampingMatrix[i] = damping(k)[i]

# ExcitationMatrix 6x1 matrix

    excitationMatrix = np.zeros((59,6,1))
    for i in range(59):
        excitationMatrix[i] = ExcitationForce(k)[i]

# PhaseMatrix 6x1 matrix

    phaseangleMatrix = np.zeros((59,6,1))
    for i in range(59):
        phaseangleMatrix[i] = PhaseAngle(k)[i]


    A = np.zeros((59,6,6))
    for i in range(59):
        A[i] = ((-(omega[i][0])**2)*(massMatrix[i]+addedmassMatrix[i])) # -w**2 (A+M)

    B = np.zeros((59,6,6))
    for i in range(59):
        B[i] = (omega[i][0])*(dampingMatrix[i])
    Bcomplex=B*cmplxNumber        # -w*i*B
#Calculate natural frequency, omegan=, remember mass and added mass

    B2 = np.zeros((59,6,6)) #add a constand for critical damping
    for i in range(59):
        B2[i]=2*np.sqrt(((massMatrix[i]+addedmassMatrix[i])*springMatrix[i]))*(frequencyMat

    C = np.zeros((59,6,6))
    for i in range(59):
        C[i] = (springMatrix[i])                              # C

    H = A + Bcomplex +B2 + Bpto() + C + Cspring()


    Fe = np.zeros((59,6,1))
    for i in range(59):
        Fe[i] = (excitationMatrix[i])*np.exp((-phaseangleMatrix[i])*cmplxNumber)
        Fefull = Fe*np.exp(cmplxNumber)

    HInverse = np.linalg.inv(H)
    z=np.zeros((59,6,1))
    for i in range(59):
        z[i] = np.dot(HInverse[i],Fe[i])
        rao= np.sqrt(((z.real)**2)+(z.imag)**2)

    x = frequencyMatrix
    y = list()
    for i in range(59):
        y.append(rao[i][2]) #Index #2 is for heave. Change the index for other DOF



    return y
RAOList.append(RAO(R, H))
```

Appendix A.3

```
"""
Created on Tue Apr 13 09:43:23 2021

@author: Grete
"""

import os
import time
import subprocess
import numpy as np
import matplotlib.pyplot as plt
import shutil

from variablesone import *
from smt.sampling_methods import LHS
from Constraint_master import centerOfGravity

num=100

h=np.linspace(1,10, num=10)
r=np.linspace(5,15, num=10)

H=[]
R=[]
for i in h:
    for j in r:
        R.append([i,j])

variables=np.array(H)


i = 0

for i in range(num):
    os.chdir(r'C:\\SALOME-9.5.0\master')

    Rstr = str(Hnew[i][0])
    Hstr = str(Hnew[i][1])
    R = Hnew[i][0]
    H = Hnew[i][1]


    cog= str(-(centerOfGravity(R, H, t)))


    # Changes the variables of the geometry
    if i == i:
        a_file = open("bullet_master.py", "r")
        list_of_lines = a_file.readlines()
        list_of_lines[25] = "R = " + Rstr + "\n"
        list_of_lines[26] = "H = " + Hstr + "\n"


        a_file = open("bullet_master.py", "w")
        a_file.writelines(list_of_lines)
        a_file.close()

        b_file = open("Constraint_master.py", "r")
        list_of_lines1 = b_file.readlines()
        list_of_lines1[27] = "R = " + Rstr + "\n"
```

```
list_of_lines1[28] = "H = " + Hstr + "\n"

b_file = open("Constraint_master.py", "w")
b_file.writelines(list_of_lines1)
b_file.close()

c_file = open("matrix.py", "r")
list_of_lines2 = c_file.readlines()
list_of_lines2[12] = "R = " + RR + "\n"
list_of_lines2[13] = "H = " + HH + "\n"

c_file = open("matrix.py", "w")
c_file.writelines(list_of_lines2)
c_file.close()

# Changes directory, so the new geometry can be runned in SALOME and creates a .dat"
os.chdir(r'C:\\SALOME-9.5.0')

print ('Run Salome')
output = subprocess.run("run_salome.bat -t master\\bullet.py", capture_output=True).std
print (output)

subprocess.run("kill_salome.bat", shell=False)

# Checks if the new dat file is created. If so the name of the file is renamed to "Name
print('DAT file is created')
if os.path.exists('master/bullet.dat'):
    os.rename('master/bullet.dat','master/bullet' + str(i) + '.dat')
    print("")


# Changes directory in order to get the .cal fil for NEMOH simulation as well as update
os.chdir(r'C:\\SALOME-9.5.0\master')
if i == i:
    d_file = open("s2n.py", "r")
    list_of_lines4 = d_file.readlines()
    list_of_lines4[14] = "R = " + RR + "\n"
    list_of_lines4[15] = "H = " + HH + "\n"


    d_file = open("s2n.py", "w")
    d_file.writelines(list_of_lines4)
    d_file.close()

print('Starting s2n')
from s2n import salome2Nemoh
filename = "bullet" + str(i) + ".dat"
symmetryXZ = "no"
nodesNPanels = salome2Nemoh(filename, symmetryXZ, cog)

# Checks if the nemoMesh.dat file is created from salome2nemohscript
if os.path.exists('nemohMesh.dat'):
    print ('Salome2Nemoh is Finished')
    print ('Start NEMOH')

    # Runs Nemoh calculation for "Name(num)" file
    runpreProcessor = subprocess.run("preProcessor.exe")
    print('PreProcess')
    runSolver = subprocess.call("Solver.exe")
    print('Process')
    runpostProcessor = subprocess.run("postProcessor.exe")
```

```
print('PostProcess')
print(RR)
print(HH)

# Calculates all the hydrodynamic responses from NEMOH output files
if os.path.exists('Results/RadiationCoefficients.tec'):
    print('Salome2Nemoh Finished!')
    os.rename("Results",("Results" + str(i)))
    os.rename("Mesh",("Mesh" + str(i)))

    # Creates new directories for the next NEMOH calculation
    if os.path.isdir("Results" + str(i)):
        os.mkdir("Results")
        os.mkdir("Mesh")


        shutil.move("Normalvelocities.dat", "Results" + str(i) + "/Normalvelocities


        shutil.move("nemohMesh.dat", "Results" + str(i) + "/nemohMesh.dat")


        shutil.move("ulletmaster" + str(i) + ".dat", "Results" + str(i) + "/bullet"


        shutil.copyfile("Nemoh.cal", 'Results' + str(i) + "/Nemoh" + str(i) + '.cal
```

Appendix A.4

```
# -*- coding: utf-8 -*-
"""
Created on Fri Mar 19 12:14:11 2021

@author: Grete
"""

# -*- coding: utf-8 -*-


#from rao_test2 import RAO
import math
from scipy.integrate import quad
import matplotlib.pyplot as plt
import numpy as np

x1 = 0.1 #Start omega
x2 = 3.0 #Stop omega

Hs_Values = np.array([float(x)/10 for x in range(int(5), int(50), 10)])
Tp_Values = np.array([float(x)/10 for x in range(int(30), int(110), 10)])
p = 1025 # Sea Water Density
g = 9.81 # Gravity

gammap = 3.3

def hstpList():
    value_list = list()

    i = 0
    for Hs in Hs_Values:
        for Tp in Tp_Values:
            value_list.append(S(Hs, Tp))
            i += 1

    return value_list



def S(Hs, Tp):
    omega_liste = [float(x)/100 for x in range(int(x1*100), int(x2*100), 2)]  # En liste over a

    value_list = list()

    omegap = 2*(math.pi/Tp)
    for omega in omega_liste:
        if omega < omegap:
            sigma = 0.07
        else:
            sigma = 0.09
        A = math.exp(-(((omega / omegap) - 1) / (sigma * math.sqrt(2)))**2)

        Sw = 0
        if omega != 0:
            Sw = ((320*((Hs**2)/Tp**4))*(omega**(-5))) * math.exp(((-1950)/Tp**4)*omega**(-4))
        values = (omega, sigma, A, Sw, Hs, Tp)  # Tuple
        # Thet tuple contain information about omega and the corresponding values for sigma, A

        value_list.append(values)  # Lagrer hele tuppelen i listen "verdi_liste"

    return value_list
```